Nano-Engineered Contrast Agents

Toward Multimodal Imaging and Acoustophoresis

Satya V. V. N. Kothapalli

Doctoral Thesis

Department of Medical Engineering
School of Technology and Health
KTH - Royal Institute of Technology
141 52 Huddinge, Sweden

Abstract

Diagnostic ultrasound (US) is safer, quicker and cheaper than other diagnostic imaging modalities. Over the past two decades, the applications of US imaging has been widened due to the development of injectable, compressible and encapsulated microbubbles (MBs) that provide an opportunity to improve conventional echocardiographic imaging, blood flow assessment and molecular imaging. The encapsulating material is manufactured by different biocompatible materials such as proteins, lipids or polymers. In current research, researchers modify the encapsulated shell with the help of advanced molecular chemistry techniques to load them with dyes (for fluorescent imaging), nanoparticles and radioisotopes (for multimodal imaging) or functional ligands or therapeutic gases (for local drug delivery). The echogenicity and the radial oscillation of MBs is the result of their compressibility, which undoubtedly varies with the encapsulated shell characteristics such as rigidity or elasticity.

In this thesis, we present acoustic properties of novel type of polyvinyl alcohol (PVA)-shelled microbubble (PVA-MB) that was further modified with superparamagnetic iron oxide nanoparticles (SPIONs) to work as a dual-modal contrast agent for magnetic resonance (MR) imaging along with US imaging. Apparently, the shell modification changes their mechanical characteristics, which affects their acoustic properties. The overall objective of the thesis is to investigate the acoustic properties of modified and unmodified PVA-MBs at different ultrasound parameters.

The acoustic and mechanical characterization of SPIONs modified PVA-MBs revealed that the acoustical response depends on the SPION inclusion strategy. However they retain the same structural characteristics after the modification. The modified MBs with SPIONs included on the surface of the PVA shell exhibit a soft-shelled behavior and produce a higher echogenicity than the MBs with the SPIONs inside the PVA shell. The fracturing mechanism of the unmodified PVA-MBs was identified to be different from the other fracturing mechanisms of conventional MBs. With the interaction of high-pressure bursts, the air gas core is squeezed out through small punctures in the PVA shell. During the fracturing, the PVA-MBs exhibit asymmetric (other modes) oscillations, resulting in sub- and ultra-harmonic generation. Exploiting the US imaging at the other modes of the oscillation of the PVA-MBs would provide an opportunity to visualize very low concentrations of (down to single) PVA-MBs. We further introduced the PVA-MBs along with particles mimicking red blood cells in an acoustic standing-wave field to observe the acoustic radiation force effect. We observed that the compressible PVA-MBs drawn toward pressure antinode while the solid blood phantoms moved toward the pressure node. This acoustic separation method (acoustophoresis) could be an efficient tool for studying the bioclearance of the PVA-MBs in the body, either by collecting blood samples (in-vitro) or by using the extracorporeal medical procedure (ex-vivo) at different organs.

Overall, this work contributes significant feedback for chemists (to optimize the nanoparticle inclusion) and imaging groups (to develop new imaging sequences), and the positive findings pave new paths and provide triggers to engage in further research.

Keywords: Nano-engineered microbubbles; SPION nanoparticles; Acoustic characterization of MBs; Fracturing mechanism of MBs; Opto-acoustics; Acoustophoresis

Sammanfattning

Diagnostiskt ultraljud (UL) är säkrare, snabbare och billigare än andra bildgivande system. Användningsområdena för diagnostiskt UL har under de senaste två decennierna ökat avsevärt tack vare utvecklingen av injicerbara mikrobubblor (MBs) som förbättrar bildkvaliteten, möjliggör för detektion av blodflöden samt molekylär avbildning. MBs stabiliseras av ett skal bestående av biokompatibla material såsom proteiner, lipider eller polymerer. Framtida användningsområden för MBs är fluorescent -, multimodal-, samt målspecifik avbildning, vilket kan uppnås genom att binda in fluorescenta partiklar, nanopartiklar, isotoper och terapeutisk gas till skalet. MBs är komprimerbara, vilket ger upphov till ett radiellt svängningsmönster som resulterar i hög ekogenicitet. Dock påverkas komprimerbarheten av skalets styvhet och elasticitet.

I den här avhandlingen presenteras en ny typ av MB (PVA-MB) som stabiliseras av ett skal av polyvinylalkohol (PVA). Genom att modifiera bubblorna med magnetiska partiklar (SPIONs) kan PVA-MB avbildas med både ultraljud och magnetisk resonanstomografi (MR). Modifieringen av skalet innebär dock en förändring av MBs mekaniska egenskaper, vilket påverkar deras akustiska egenskaper. Syftet med denna avhandling är därför att undersöka hur MBs akustiska egenskaperna påverkas av skalmodifieringen.

Akustiska och mekaniska undersökningar av skalmodifierade PVA-MBs avslöjade att den akustiska responsen beror på inklusionsstrategin av SPIONs, dock påverkas inte MBs strukturella egenskaper. De modifierade MBs med SPIONs bundet till PVA-skalets yta uppvisar ett mjukt skalbeteende och ger därför högre respons än de mer stela MBs med SPIONs inuti PVA-skalet. När bubblorna utsätts för ett högt akustiskt tryck börjar skalet att spricka. Det visade sig dock att sprickbildningen av den omodifierade PVA-MB skiljer sig jämfört med konventionella MBs. När PVA-MB utsätts för ett högt akustiskt tryck börjar den inneslutande gasen att sippra ut genom små hål i PVA-skalet. I samband med detta börjar PVA-MB att svänga asymmetriskt, vilket genererar sub- och ultraharmoniska frekvenser. Genom att utnyttja detta svängningsmönster kan man konstruera UL sekvenser som har förmågan att detektera låga koncentrationer (ner till enskilda) PVA-MBs. Vi har även introducerat PVA-MBs tillsammans med partiklar som efterliknar röda blodkroppar i ett akustiskt fält för att observera effekten av acoustic radiation force strålkraftseffekten. Vi observerade att de komprimerbara PVA-MBs drogs till antinoden medan blodfantomerna bestående av fast materia rörde sig mot trycknoden. Den här akustiska separationen (acoustophoresis) kan vara ett effektivt verktyg för att studera bioclearance av PVA-MBs ut ur kroppen antingen genom att samla in blodprover (in vitro-studie) från olika organ eller genom att använda ex-vivo-metoder.

Denna avhandling ger värdefull återkoppling till kemisterna i deras arbete kring att optimera inbindningen av nanopartiklar till skalet, men även för utveckling av nya bildsekvenser som kan förbättra förmågan att avbilda låga koncentrationer av PVA-MBs.

PREFACE AND ACKNOWLEDGEMENT

This doctoral thesis work was carried out at the Department of Medical Engineering, School of Technology and Health (STH), Royal Institute of Technology-KTH, Stockholm, Sweden under the guidance of Dr. Dmitry Grishenkov and Prof. Lars-Åke Brodin. This study was performed as part of the 3MiCRON (Three modality contrast imaging using multi-functionalized microballoons) project funded by the European Commission within the 7th Framework Programme (FP7-NMP-2009-LARGE-3, 2010-2013). The doctoral thesis is to be publicly defended on Tuesday 22nd September, 2015, from 09:00 am to 12:00 am, in lecture hall 3221, Alfred Nobels Allé 8, Huddinge, Sweden.

This page is the right place to express my gratitude to several people who have inspired me directly or indirectly to reach this stage. First and foremost, I would like to express my gratitude to my supervisor, Lars-Åke Brodin, who paved the path for my research career. I always owe him for giving me an opportunity, and I still remember our first meeting, which was an unbelievable moment like climbing Everest. I would also express my greatest appreciation to my supervisor, Dmitry Grishenkov, for his extensive support, for his critiques, and for sharing his knowledge and office. You are very admirable. Спасибо за ваш замечательный поддержки. I would like to acknowledge Birgitta Janerot-Sjoberg for her through proofreading and brilliant feedback.

My gratitude is also expressed to the EU Commission for their financial aid and great support for the 3MiCRON project. I thank all of my partners (Universitadeglistudidi Roma Tor Vergata, University College Dublin, KarolinskaInstitutet, FondazzioneIRCCS–InstitutoNazionaledeiTumori, SurflayNanotecGmbH, UniversitaetBayreuth, EsaoteSPA, StifelsenSintef, Deutsches Krebsforschungszentrum) and collaborators (Erasmus MC and Royal Institute of Technology, KTH) for sharing their labs, knowledge and techniques. I offer special thanks to Karen Gustafsson and Peta Sjölander for their supporting management issues during the 3MiCRON project. I would also like to extend my gratitude to Kenneth Caidahl for sharing his knowledge by arranging special meetings, Gaio Paradossi for providing the "magical Italian bubbles", and Björn Gustafsson, Silvia Margheritelli, Letizia Oddo, Melanie Poehlmann, Claudia Sciallero, Rune Hansen, and Åsa Barrefelt for being good friends and sharing fun ideas during the 3MiCRON meetings. I would also like to express my appreciation to Verya Daeichin and Nico de Jong for providing an opportunity to capture the "mysterious bubble" oscillation. I offer special thanks to Martin Wiklund for his wonderful support, for constructive discussions, and for letting me conduct the research for my final article in his lab.

I would also like to express my appreciation to Anna Bjällmark, Mattias Mårtensson, and Matilda Larsson. Anna, thank you for your motivation and support during my Ph.D. studies. Mattias, thank you for your role in pushing me to perform the work in time. Matilda Larsson, thank you for the support, fun and it was a pleasure and fun, especially in the Genova and Berlin project meetings and in Prague for the IEEE Symposium. I would also like to offer my gratitude to Hamed Hamid Muhammed for his supervision, support

LIST OF INCLUDED PAPERS

1. Brismar, T. B., Grishenkov, D., Gustafsson, B., Härmark, J., Barrefelt, Å., **Kothapalli, S. V.**, ... & Paradossi, G. (2012). Magnetite nanoparticles can be coupled to microbubbles to support multimodal imaging. *Biomacromolecules*,*13*(5), 1390-1399.

2. Sciallero, C., Grishenkov, D., **Kothapalli, S. V.**, Oddo, L., & Trucco, A. (2013). Acoustic characterization and contrast imaging of microbubbles encapsulated by polymeric shells coated or filled with magnetic nanoparticles. *The Journal of the Acoustical Society of America*, *134*(5), 3918-3930.

3. Poehlmann, M., Grishenkov, D., **Kothapalli, S. V.**, Härmark, J., Hebert, H., Philipp, A., ... & Fery, A. (2014). On the interplay of shell structure with low-and high-frequency mechanics of multifunctional magnetic microbubbles. *Soft matter*, *10*(1), 214-226.

4. **Kothapalli, S. V.**, Oddo, L., Paradossi, G., Brodin, L. Å., & Grishenkov, D. (2014). Assessment of the Viscoelastic and Oscillation Properties of a Nano-engineered Multimodality Contrast Agent. *Ultrasound in medicine & biology*,*40*(10), 2476-2487.

5. **Kothapalli, S. V.**, Daeichin, V., Mastik, F., Brodin, L. A., Janerot-Sjoberg, B., Paradossi, G., ... & Grishenkov, D. (2015). Unique pumping-out fracturing mechanism of a polymer-shelled contrast agent: an acoustic characterization and optical visualization. *Ultrasonics, Ferroelectrics, and Frequency Control, IEEE Transactions on*, *62*(3), 451-462.

6. **Kothapalli S, V. V. N.**, Wiklund, M, Janerot-Sjöberg, B, Brodin, L. Å., and Grishenkov, D, Investigation of Polymer-shelled Ultrasound Contrast Agents in Acoustophoresis, submitted to Ultrasonics (2014).

Division of Work between Authors

Paper 1. This paper includes contribution from 5 research groups: Department of Radiology, Karolinska Institute (KI); Department of Medical Engineering, KTH; Department of Molecular Medicine and Surgery, KI; Department of Structural Biology, KTH; Department of Chemical Science and Technology; University of University of Rome Tor Vergata (UNITV). In this paper, **Kothapalli** and Grishenkov were responsible for the assessment of the acoustic properties of dual modal contrast agents. **Kothapalli** performed experiments (backscattered power and attenuation coefficient), and Grishenkov did the scientific writing part.

Paper 2. This paper is contribution from two research groups: Department of Electrical, Electronic, Telecommunication Engineering and Naval Architecture, University of Genoa; Department of Medical Engineering, KTH; study was designed by **Kothapalli** and Grishenkov and experiments and scientific writing part was done by **Kothapalli** under the supervision of Grishenkov.

Paper 3. This paper is the contribution of three research groups: University of Bayreuth (UBT), Physical Chemistry II; Department of Medical Engineering, KTH; Department of Structural Biology, KTH; within the 3MiCRON project. In this paper, **Kothapalli** and Grishenkov were responsible for the assessment of shell mechanical properties through modeling. **Kothapalli** did both acoustical experiments and simulations, and Grishenkov did the scientific writing.

Paper 4. In this paper, **Kothapalli** performed the experiments, and Kothapalli did scientific writing under the supervision of Grishenkov.

Paper 5. In this paper, **Kothapalli** together with Daeichin and Grishenkov performed the experiments, and Kothapalli did scientific writing under the supervision of Grishenkov.

Paper 6. In this paper, **Kothapalli** performed experiments together with Grishenkov at the department Cell Physics, KTH. **Kothapalli** analyzed the video clips, and the scientific writing was conducted under the supervision of Grishenkov and Wiklund.

OTHER SCIENTIFIC CONTRIBUTIONS

I. **Kothapalli, V. V. S. N.**, Grishenkov, D., Brodin, L. Å., & Paradossi, G. (2011). Coded Excitation Technique in Detection of Polymeric-Shelled Ultrasound Contrast Agents: in Vitro Study. In *8th International Conference on Nanosciences & Nanotechnologies (NN11) 12-15 July 2011, Thessaloniki, Greece.: Workshop: NANOMEDICINE*

II. **Kothapalli, S. V.**, & Grishenkov, D. (2012). Optimization of Driving Pulse Envelope in Detection of Harmonic Response from a Lipid-Shelled Ultrasound Contrast Agent. In *19th International Congress on Sound and Vibration 2012, ICSV 2012: Volume 3, 2012* (pp. 1882-1889).

III. **Kothapalli, S. V.**, Brodin, L. Å., Grishenkov, D., & Paradossi, G. (2013). Dynamic and Structural Behavior of Magnetic PVA-Shelled Microbubbles: Acoustic Characterization. In *2013 Joint UFFC, EFTF and PFM Symposium* (pp. 1509-1512).

IV. Poehlman, M., **Kothapalli, V. V. S. N.**, Grishenkov, D., Härmark, J., Hebert, H., Philipp, A., ... & Fery, A. (2013). Magnetic microbubbles for multimodality imaging: the importance of the shell structure for low and high frequency mechanics. In *European Symposium and exhibition on biomaterials and related areas, Euro BioMAT2013 23-24 Apr 2013 Weimar, Germany.*

V. **Kothapalli, S. V.**, Faridi, A., Wiklund, M., & Grishenkov, D. (2013). On-chip actuation of polymer shelled microbubbles. In *Medicinteknikdagarna, 1-2 October 2013, Stockholm, Sweden.*

VI. D. Grishenkov, **S.V.V.N. Kotapalli**, V. Daeichin, F. Mastik, N. de Jong. (2014). Unique Fracturing Mechanism of Polymer Shelled Microbubble: Acoustic Characterization and Optical Observation. In a *20th European Symposium on Ultrasound Contrast Imaging*, *23-24 January 2014, Rotterdam, The Netherlands.*

VI

ABBREVIATIONS

MB- microbubble

UCA-ultrasound contrast agent

PVA-poly(vinyl) alcohol

BSP-backscattering power

US-ultrasound

MR-Magnetic resonance

SPECT-single photon emission computed tomography

SPION- super-paramagnetic iron oxide nanoparticles

3MiCRON- Three modality contrast imaging using multi-functionalized microballoons

CPS-contrast pulse sequence

TEM-transmission electron microscopy

AFM- atomic force microscopy

UBT- university of Bayreuth

CLM- confocal laser microscope

CTR- contrast-to-tissue ratio

SNR- signal-to-noise ratio

ROI- region of interest

MHz- mega Hertz

kHz- kilo Hertz

Pa- Pascal

USW- ultrasound standing wave

NO- nitric oxide

TABLE OF CONTENTS

X

1. INTRODUCTION

Approximately 47 years ago, Gramiak and Shah [1] reported for the first time that microbubbles contained in an injected solution enhance the ultrasound visualization of the lumen of the aortic root. In the presence of ultrasound propagation, the compressible gas particles act as stronger echo sources than the tissue. As a result, the microbubbles markedly increase the backscattered signals in the Doppler ultrasound examination and enhance the contrast in B-mode imaging [2, 3]. The naked microbubbles produced in saline are rapidly removed from the blood fluids and the lungs due to the high surface tension [3], and the contrast-enhanced ultrasound imaging in the left cardiac chamber is difficult. As a reason, the naked microbubbles were coated with an extra protective layer, similar to balloons, to improve their blood circulation time. The encapsulated materials are typically made of protein [4], lipid [5] or polymer [6]. Currently, lipid or protein-coated MBs are approved in more than 70 countries to enhance the ultrasound imaging of hypoechoic (producing low echoes) regions, e.g., left ventricular opacification, endocardial border delineation, liver, kidney, breast, portal vein, extra cranial carotid, peripheral arteries, and macro and microvascular imaging [7]. These particles are injected intravenously, and their typical sizes are between 1-10 μm. MBs are compressible and expandable in the presence of ultrasound waves. The MBs oscillate non-spherically at high-intensity ultrasound pressures typically more than 100 kPa. The nonlinear oscillations generate higher harmonic frequencies in the frequency spectrum, which is highly unlikely to happen in tissue at those pressures [2]. This phenomenon has been exploited to develop new strategic excitation pulses combined with signal processing techniques to obtain high-resolution and low-artifact images.

Recent advances in molecular and surface chemistry have enabled the development of multipurpose MBs for molecular/therapeutic purposes (by attaching the drug ligand molecules) and to be multimodal contrast agents (by including the nanoparticle). Thus, the current generation of MBs is used for not only diagnostic purposes but also molecular imaging, site-specific drug delivery purposes, and even for multimodal contrast-enhanced imaging. In fact, the contrast-enhanced imaging technique is very much dependent on the

behavior of the MBs under ultrasound exposure. Indeed, the modified nano-engineered MBs might possess acoustic properties (dynamics) different from or the same as those of unmodified MBs [8]. Thus, it is essential to have a detailed understanding of the acoustic properties of any novel modified (nano-engineered) MBs with respect to unmodified MBs for ultrasound contrast-enhanced imaging.

In this thesis, the acoustic and mechanical properties of novel modified and unmodified polymer-shelled MBs are examined. These MBs are relatively thick and robust compared to commercially available MBs (i.e., lipid- or protein-shelled MBs). The encapsulating polymer shell is made of cross-linked polyvinyl alcohol (PVA), and the gas core is air, leading them to be referred to as PVA-MBs. The backscattering efficiency of the PVA-MBs was shown to be good enough to improve the detection of Doppler ultrasonography in small vessels [9]. It was also shown that it was possible to enhance the B-mode imaging with a good contrast-tissue-ratio (CTR) using the Chirp CPS3 (both frequency and amplitude modulation) pulse technique [10]. The outer surface of the PVA-MBs was left with the hydroxyl groups, which enables the much simpler and straightforward conjugation of drug molecules or nanoparticles [11].

In this thesis we examined the nano-engineered shelled PVA-MBs' behavior under ultrasound exposure. The acoustic properties are investigated within the 1-15 MHz frequencies and 0.1-2.5 MPa pressures. The mechanical properties are also estimated by fitting the theoretical acoustic attenuation coefficient and phase velocity data with the experimental data. We provide insights on the visual inspection of the MB dynamics using a high-speed camera called the Brandiris-128 camera [12] at a frame rate of 25 million frames/second. We visualized the translatory motion of the PVA-MBs caused by the acoustic radiation force in a standing-wave field with a regular system camera at a frame rate of 50 frames/second. The camera is coupled to a standard inverted microscope, and an acoustic standing-wave field with a frequency of 2.8 MHz was created in a microfluidic chip with an attached piezoelectric crystal (PZT).

1.1 Outline of the Thesis

This thesis work is organized into 8 chapters based on the work from 6 articles that are attached in the appendix section. After the introduction, the main objective of the thesis is stated in Chapter 2. Thereafter, a brief retrospective study of the radial oscillation of different type of MBs and their applications, and acoustophoresis applications is presented as a background in Chapter 3. Methodologies, results, discussion and conclusions based on the 6 articles are summarized in Chapter 4, 5, 6 and 7, respectively. The future perspective studies are briefly discussed in Chapter 8.

2. OBJECTIVES

The overall aim of this thesis is to investigate the backscattered signals of modified PVA-MBs, examine high-speed recordings of radial oscillation and translatory motion of unmodified PVA-MBs, and identify potential clinical applications. The specific objectives are listed below:

– To examine the acoustic properties such as scattering efficiency and acoustic absorption and the fracture pressure threshold at different acoustic pressures and different dilution rates of dual-modal contrast agents (PVA-MBs + SPIONs) (Papers 1 and 2).

– To estimate the mechanical and physical properties of modified and unmodified PVA-MBs by modeling the harmonic oscillation of PVA-MBs and fitting the theoretical attenuation coefficient and phase velocity data with measurements (Papers 3 and 4).

– To assess the fracturing behavior of PVA-MBs with the help of visualizing the radial oscillation of individual PVA-MBs and examining the backscattered echo signals from a bulk PVA-MB suspension at a high insonation pressure of approximately 1 MPa (Paper 5).

– To investigate the possibility of using PVA-MBs in acoustophoresis applications by assessing the translatory motion of PVA-MBs caused by the radiation force in ultrasound standing wave fields (Paper 6).

3. BACKGROUND

This chapter focuses on a retrospective study of the physical principles and clinical applications of ultrasound contrast agents (UCAs) and the particle manipulation caused by the acoustic radiation force in a standing-wave field.

3.1 Ultrasound imaging

Ultrasound is a pressure or mechanical wave having frequencies above the human audible range (i.e., above 20 kHz). The acoustic wave propagates between two points in a medium as particle vibration, with the primary vibrated particle carrying the acoustic energy to its neighbor particles and the neighbor particles to its next neighbor particles. This process continues until the wave energy is diminished. When the acoustic wave encounters an interface between two media with two different material properties (such as density (ρ) and speed of sound (c)), the acoustic wave is reflected. Based on the strength and timing of the reflection pulses (also known as the echo), the range of objects is located and identified [13].

Diagnostic ultrasound (sonography) imaging is obtained from the reconstruction of the echoes produced from fibrous tissue (see Figure. 1a). Diagnostic ultrasound typically operates within the 1-15 MHz frequencies, and the corresponding wavelengths are 0.1-1.5 mm. When performing ultrasound imaging at high frequencies (above 15 MHz), the acoustic wave penetrates less due to absorption, and at low frequencies (lower than 1 MHz), far organs can be visualized but low-resolution images are obtained. The brightness of the image at each point corresponds to the strength of the echo that provides information about the position of its origin within the body [13]. The energy of the ultrasound wave that is reflected at the liver to bone interface is approximately 59%, whereas at the liver to air interface, it is approximately 99.9%. Thus, most of the ultrasonic wave reflects from the gas boundary, and this strong echo results in a high contrast image in B-mode. It is difficult to diagnose gaseous organs with the ultrasound modality, but nitrogen gas bubbles in the body (due to diving sickness) are generally diagnosed by using

diagnostic ultrasound [14] because of its clear echo differentiation from other organs (such as bones and tissue). In a similar way, very tiny injectable gas particles enhance the contrast of ultrasound imaging to visualize the blood flow in the cardiac chambers (see Figure. 1b). These small micro gas particles with a protection layer are referred to as ultrasound contrast agents (UCAs).
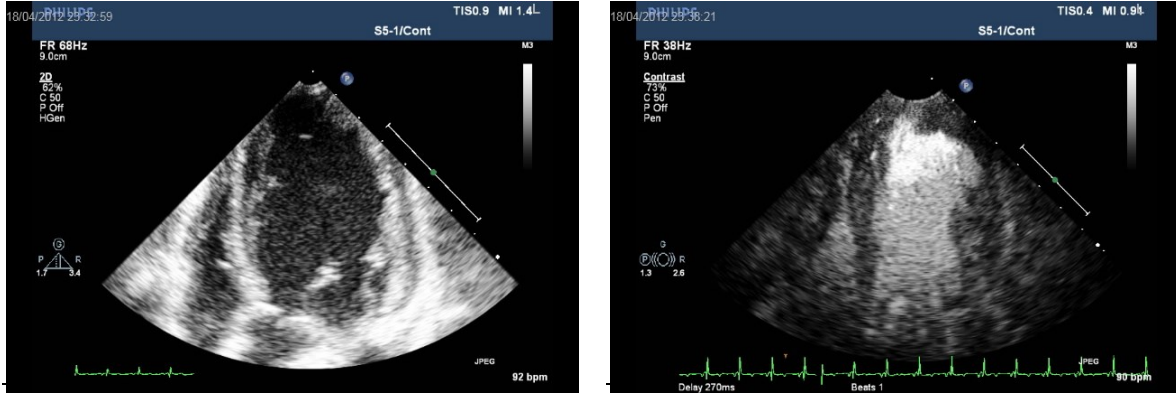
Figure 1. Two-dimensional ultrasound images of the heart, which were taken (a) before and (b) after injection of ultrasound contrast agents. These figures were reprinted with the permission of Malin Larsson at the Department of Medical Engineering, School of Technology, at the KTH Royal Institute of Technology. The tissue consists of highly non-homogeneous fibrous material, so it has more scatters/volume. Hence, the tissue appears brighter (hyper-echogenic). However, blood (consists of blood cells and blood plasma) is an approximately homogenous material, which has fewer scatters/volume. Thus, the blood appears dark (hypo-echoic) in the ultrasound B-mode image in (a). In (b), the brightness and contrast of the heart cavity is increased with the arrival of the gas bubbles. Note that the contrast of the image depends on the difference in scatters available in the insonified volume.

3.2 Ultrasound contrast agents

The story of UCAs was started back in 1967 [1], where tiny free gas MBs were visualized as very bright scatters in the blood pool during the echocardiography examinations. The scattering efficiency of the MBs is explained with the help of Eq. 1,

$$\sigma_S = 4\pi R_0^2 (kR_0)^4 \left\{ \left[\frac{\beta_d - \beta_0}{\beta_0} \right]^2 + \frac{1}{3} \left[\frac{3(\rho_d - \rho_0)}{\rho_0} \right]^2 \right\},$$

(1)

where σ_S is the scattering cross section, R_o is the particle radius, k (=$2\pi/\lambda$) is the wave-number, λ is the wavelength of the acoustic wave, β_d (=7.65×10^{-6}) and β_0 (=4.4×10^{-10}) are the compressibilities of the particle and surrounding media, and ρ_d (=1.2) and ρ_0 (=1000) are the densities of the particle and surrounding media, respectively. Note that the above formula applies only when the diameter of a spherical particle is less than the 1/10 of the wavelength (λ) of the incidental acoustic wave and the frequency (f) is well below the resonance frequency (f_0) of the particle [15]. From this formula, it is evident that the scattering efficiency of the particle is proportional to the 6th power of its radius and the 4th power of the driving frequency. For example, a 3-micron sized gas bubble excited at a 2 MHz frequency generates a scattering efficiency approximately 10^8 times higher than that of a blood cell.

Even today, tiny gas bubbles produced in agitated saline are used to monitor the right cardiac insufficiency and intra-cardiac and cavity shunts [16]. This method is fast and economical, but free gas bubbles are dissolved quickly in the surrounding blood due to the high surface tension. The surface tension is equal to the pressure difference, ΔP, multiplied by the radius, R_o, of the bubble. For example, a 3 μm sized microbubble dissolves in blood in approximately 0.02 s [17]. If they are administered intravenously, they disappear before reaching the left ventricular cavity [3, 18]. Hence, it is not possible to use them in the left chamber, coronary circulation, or arterial organ evaluation. In addition to their lack of stability, it is also difficult to control their size distribution.

Free gas bubbles were encapsulated with biocompatible and biodegradable materials (such as human albumin protein [4], phospholipid[5] or polymer [6]) (see Figure. 2) to improve their circulation period. This encapsulation method reduces the surface tension and prolongs the blood circulation period compared to free gas bubbles. It enables monitoring the left cardiac chamber [19].
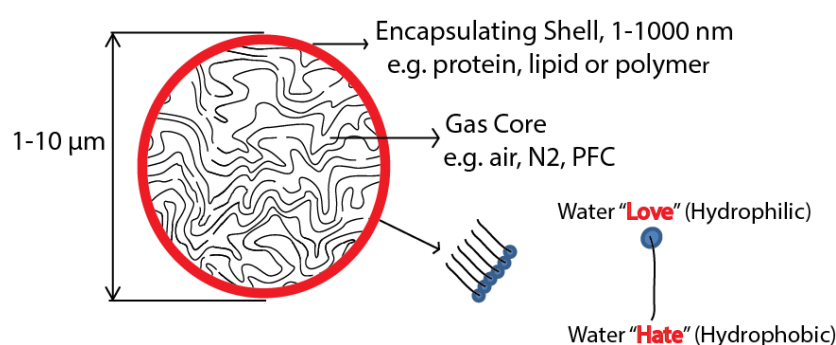
Figure 2. Schematic sketch of a typical ultrasound contrast agent.

Currently, lipid and protein-shelled MBs, such as SonoVue® (Bracco SpA), Definity® (Lantheus Medical Imaging), Optison (GE Healthcare), and Sonozoid (Amersham Health), have been approved by medical agencies in the US and Europe for diagnostic use. They are used in approximately 70 more countries for ultrasound contrast-enhanced applications, mainly for left ventricular opacification, endocardial border delineation and Doppler applications [7]. The size of the ultrasound contrast agents should be below 10 μm so as not to obstruct blood flow in the pulmonary capillaries [20] and should be above 0.1 μm to avoid leakage across the vessel wall [21]. The shell thickness of both the protein and lipid-shelled MBs are in the range of 1-15 nm, i.e., the ratio of the shell thickness to the radius of the gas core is less than 5 % [15]. Moreover, above a 0.3 mechanical index, MI, biological effects were observed such as premature ventricular contraction, microvascular rupture and petechial hemorrhage [22]. The MI is the ratio between the peak negative pressure (p_{neg}) at the investigated volume and the square root of the frequency of the incidental acoustic wave, f, i.e., MI=$\left(p_{neg} \big/ \sqrt{f} \right)$.

To address these problems, thicker and more robust polymer-shelled MBs were proposed, with polymer shell thicknesses ranging between 100-1000 nm [23]. Although thick polymer-shelled MBs prevent gas core diffusion, their echogenicity is significantly reduced compared to protein/lipid-shelled UCAs [15].

3.3 Radial oscillation of MBs at different pressures

Apart from the high scattering efficiency, highly compressible MBs can also expand and contract in the alternating acoustic pressure wave. The encapsulated MBs oscillation are significantly different from those of free gas bubbles and can be broadly classified into three types based on the incidental acoustic pressure [2, 19] (see Figure. 3).

3.3.1. Linear oscillations

At low acoustic pressures (typically below 100 kPa), a MB oscillates in a linear fashion with frequencies similar to the driving frequencies. In this regime, baseline B-mode and Doppler examinations are performed [19].
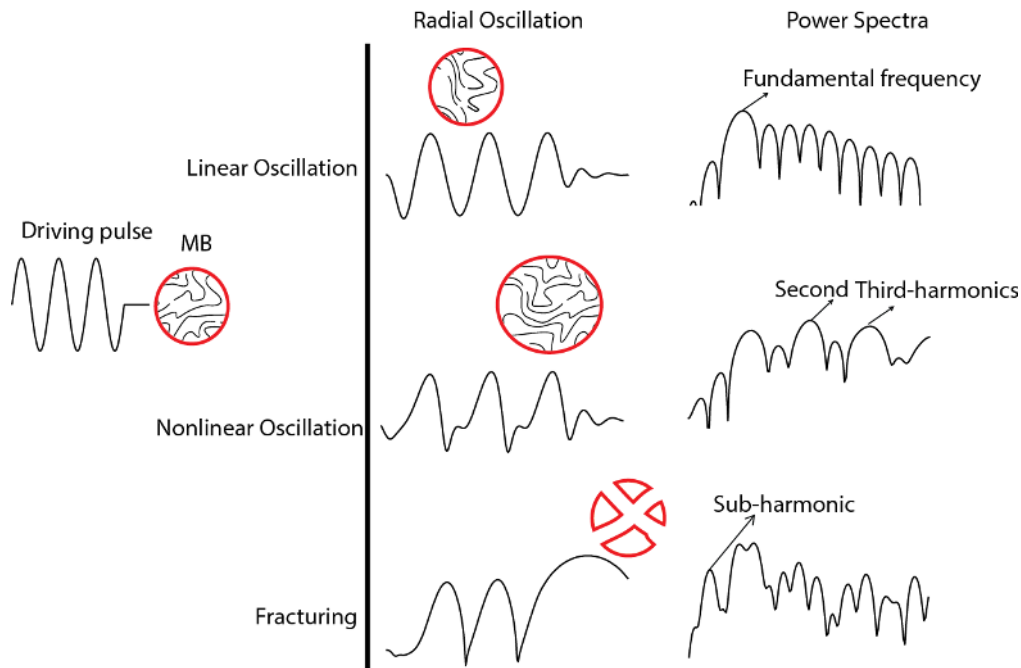
Figure 3. Schematic diagram representing the interaction of an UCA with the acoustic pressure. The left panel is the incidental pulse in the time domain, the middle panel is the scattered signals from the MBs at different pressures in the time domain, and the right panel is the frequency domain of the scattered signal from the MB.

3.3.2 Non-linear oscillation

As the incidental acoustic pressure increases (above 100 kPa), asymmetric oscillations occur in which the MB expansion is greater than the compression. This is due to the repulsion forces between the encapsulated shell molecules in the compression phase. This asymmetric (nonlinear) oscillation consequently produces integer multiples of the driving frequency (higher harmonics) [15, 19, 24]. At the above-mentioned acoustic pressure, asymmetric oscillations are not likely to happen in soft tissue, and the most of the backscattering power of the tissue is contributed at the fundamental frequency. Thus, imaging at higher harmonics that remove the tissue contribution will improve the contrast-to-tissue ratio (CTR). In the past decade, several signal processing techniques (such as pulse inversion [25], power modulation [26], contrast pulse sequences [27], power pulse inversion [28], and coded excitation techniques [29]) were implemented to remove the tissue responses and detect the harmonics produced by UCAs.

For an example, in the pulse inversion technique, two identical pulses with a 180° phase difference are transmitted to obtain the image. The linear response of the tissue provides a similar response as incidental subsequent pulses, and the sum of these two backscattered echoes cancel out the two responses. Due to the nonlinear response in the UCAs, the resulting two backscattered signals are not identical as in the tissue, and the two pulses do not cancel each other out (see Figure. 4). The resulting nonlinear signal from the UCAs improves the CTR [25].
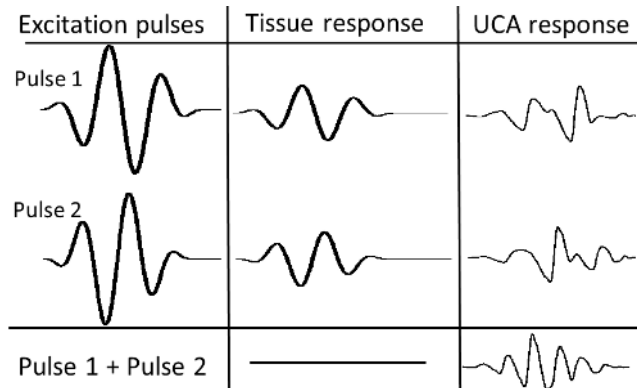
Figure 4. Result of pulse-inversion technique to cancel out the linear responses and acquire non-linear responses from MBs.

3.3.4 Other modes of oscillation

The buckling modes of oscillation, which are observed in phospholipid-shelled MBs, are characterized by the MBs being more compressed than expanded at a very low acoustic pressure of approximately 30 kPa. This generates sub and ultra-harmonics, and the magnitude of the sub-harmonic peak is higher than the second harmonic peak [17]. This buckling mode of oscillation at low acoustic pressure is proposed to monitor carotid imaging with high resolution and high CTR [30].

3.3.5 Disruption

At a high enough incidental acoustic pressure (between 0.3-1 MPa), the UCAs can be disrupted, and the gas core escapes to the surrounding media (see Figures. 3 and 6). The interaction of the ultrasound burst with the released gas causes the production of transient broadband echoes [15, 19]. The transient disruption phenomenon is used in harmonic-triggered imaging to find myocardial abnormalities [31] and in intermittent perfusion imaging to quantify tissue blood flow [32]. In the particular case of polymer-shelled MBs, the polymer shell is intact after the MB disruption, which is further used pre-clinically in ultrasound-triggered drug delivery applications [33, 34]. In addition, the assessment of the inertial cavitation of UCAs can be used in the evolution of potential bio-effects [35], and the stable cavitation (or non-inertial cavitation) of UCAs is used to perform reversible sonoporation (acoustic opening of the cell plasma membrane for the purpose of large gene molecule delivery) [36] and opening of the blood-brain barrier [37].

3.3.6. Other parameters influencing the oscillations of MBs

In addition to pressure, other acoustical parameters (such as driving frequency, number of cycles per pulse, pulse repetition frequency (PRF), and pulse shape), MB parameters (such as shell thickness and material), and physical parameters (such as temperature and static overpressure) can also influence the radial oscillation of the MBs. For example, the shell damping and the resonance frequency (where the maximum oscillation occurs) of the UCAs increase with the shell thickness and stiffness of UCAs. The resonance frequency of

thin-shelled MBs (both protein/lipid-shelled MBs) is between 1-5 MHz [17], which is in the typical clinical operation range [15], and the resonance frequency in thick-shelled MBs is usually between 5-15 MHz [9, 15]. Thus, to obtain prominent radial oscillation in polymer-shelled MBs, high-frequency (between 5-15 MHz) ultrasound transducers should be employed. As the temperature increases, the stiffness of the phospholipid-shelled MBs decreases [38], so that they can be disrupted well below their pressure threshold. The number of cycles in the pulse also influences the radial oscillation of the microbubbles. Grishenkov et al. [9] showed that as the number of cycles in the pulse increases, the fracture pressure threshold decreases.

3.4 High-speed recordings of MBs oscillation

The radial oscillations of the MBs occur in microseconds because clinical diagnostic ultrasound uses frequencies within 1-15 MHz. To visualize these micro scale oscillations, a Brandaris-128 camera [12] coupled to an ultrasound probe is used with a speed of 25 million frames/second. Direct visualization of the MB oscillations helps elucidate their behavior and can be used to construct the 1D radial oscillation (see Figure. 5). These radial oscillations are used in an appropriate physical model to obtain the encapsulated shell's mechanical parameters such as viscosity and elasticity [24, 39]. Capturing the MBs radial oscillations at high pressures also reveals the fracturing mechanism and the MBs behavior, which is an important factor for designing the pulse sequences for intermittent ultrasound imaging applications and drug delivery applications [40, 41].
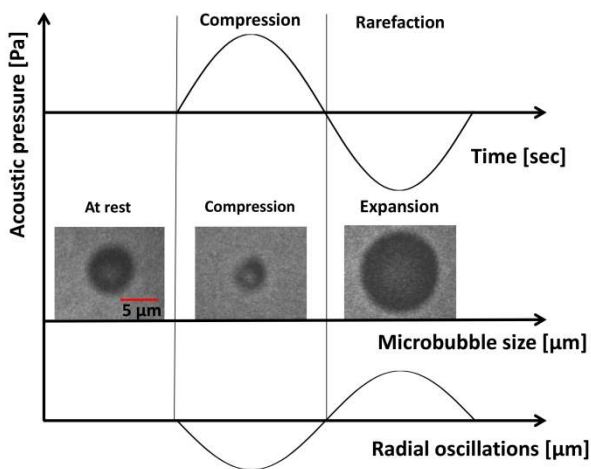
Figure 5. Illustration of radial oscillation of microbubbles upon insonation.

In previous studies, it was observed that different MBs fracture in different manners. For example, thin (phospholipid)-shelled MBs fracture above 0.3 MI, and they exhibit greater expansion (more than five times their original radius) before fracture. After fragmentation, the gas core forms new small free gas MBs, which last for several seconds in acoustic fields [42]. On the other hand, thick (polymer)-shelled MB fractures initiate at a small crack through which the gas core escapes, forming a larger free gas bubble that attaches to the PVA shell (see Figure. 6). The naked gas bubbles again last for some time in the ultrasound field, and the shell remains intact after the gas extrusion [33, 43]. Recently, a shedding behavior (i.e., the bubble mass is gradually drained out) was identified in lipid-shelled MBs when they were exposed to a series of insonation pulses just below the fracture pressure threshold [44]. This shedding behavior was proposed to be useful in combined drug delivery applications for monitoring the therapeutic effect at low acoustic pressures [45].

All of the facts mentioned above illustrate the particular importance and clinical relevance of not only identifying the rupture pressure threshold but also understanding the fracture mechanism of the UCAs.

Note: With the Brandaris-128 camera, we can focus on and capture only the single (or at maximum, very few) microbubble oscillations.
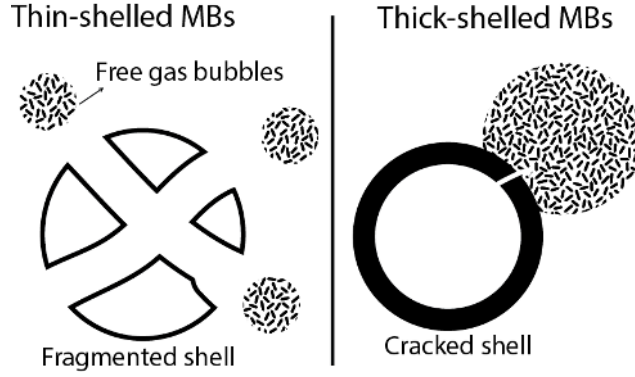
Figure 6. Schematic sketches of the fracturing behavior of (a) thin and (b) thick-shelled microbubbles.

3.5 Modeling

The fundamental mathematical expression of the dynamics of a naked gas bubble were derived by Lord Rayleigh and Plesset and extended by Noltingk-Neppiras-Poritsky as the RPNNP equation. The RPNNP nonlinear equation of motion (NEM) of a gas bubble was formulated based on Newton's third law, which states that the force acting on a surface (liquid pressure and driving pressure) equals the force acting in the bubble (gas pressure) [39]. The resultant NEM of a gas bubble is given in Eq. 2.

$$\rho_L \left(R\ddot{R} + \frac{3}{2}\left(\dot{R}\right)^2 \right) = p_G \left(\frac{R_0}{R}\right)^{3k} - 4\mu_L \frac{\dot{R}}{R} - \frac{2\sigma}{R} - p_v - p_\infty.$$

$$(2)$$
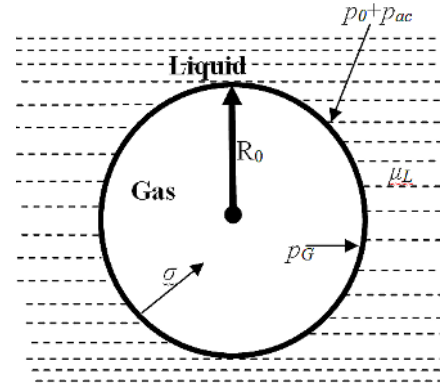
Figure 7. Schematic representation of a free gas bubble, which is adopted from [46].

The left side terms represent the inertia of the surrounding liquid against the oscillating bubble; $4\mu_L \dfrac{\dot{R}}{R}$ represents the damping in the liquid, whereas the other terms represent restoring forces; ρ_L is the density of the surrounding liquid; R is the instantaneous gas bubble radius, which varies with the time, t, during the oscillation; the dots on top of the R

represent the differentiation with respect to time; p_∞ denotes the sum of the ambient, p_o, and incidental, $p_{ac}(t)$, pressures; μ_L is the shear viscosity of the surrounding liquid; p_G is the gas pressure at equilibrium; σ is the surface tension; and k is the polytrophic gas constant, which varies between the isothermal state (when the ratio of specific heats, γ, =1) and the adiabatic state (when γ=1.4).

In the case of encapsulated MBs, the model should include the contributions of both the damping and elasticity of the encapsulating layer (see Figure 8). Roy et al. derived the NEM for an encapsulated MB, where the encapsulating shell was assumed to be a simple viscous liquid. In a similar approach, de Jong et al. [47] derived the NEM of a protein-shelled MB, in which the shell surface's elastic modulus and viscosity parameters were included in the RPNNP NEM to counterbalance the shell.

$$R_1 \ddot{R}_1 \left(1 + \frac{\rho_L - \rho_S}{\rho_S} \frac{R_1}{R_2} \right) + \left(\dot{R}_1 \right)^2 \left(\begin{array}{c} \frac{3}{2} + \left(\dfrac{\rho_L - \rho_S}{\rho_S} \right) \\ \times \left(\dfrac{4R_2^3 - R_1^3}{2R_2^3} \right) \dfrac{R_1}{R_2} \end{array} \right) =$$

$$\frac{1}{\rho_S} \left[\begin{array}{c} P_{G,eq} \left(\dfrac{R_{01}}{R_1} \right)^{3\kappa} - P_\infty(t) - 4\mu_L \dfrac{R_1^2 \dot{R}_1}{R_2^3} \\ - 2\dfrac{(\sigma_1 + \sigma_2)}{R} + 3 \displaystyle\int_{R_1}^{R_2} \dfrac{\tau_{rr}^S(r,t)}{r} dr \end{array} \right] ,$$

(3)
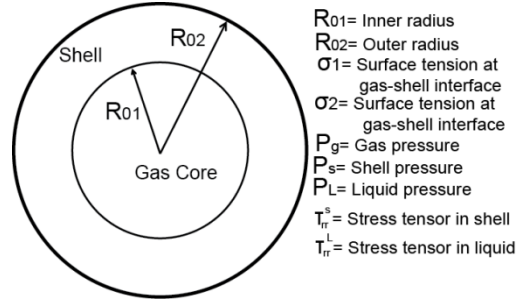
Figure 8. Schematic representation that shows the forces acting on the microbubble shell surface.

R_{01}= Inner radius
R_{02}= Outer radius
σ_1= Surface tension at gas-shell interface
σ_2= Surface tension at gas-shell interface
P_g= Gas pressure
P_s= Shell pressure
P_L= Liquid pressure
τ_{rr}^s= Stress tensor in shell
τ_{rr}^L= Stress tensor in liquid

Several models have been derived based on the above NEM equation by including different assumptions according to the acoustical behavior of microbubbles. Church [48] was developed a model that includes the Kelvin-Voigt constitutive equation (where the shell is assumed to be a viscoelastic solid) in the NEM of a gas bubble (see Eq. 3). The Church model is flexible and can be used for a variable shell thickness, so several NEMs of UCAs were used the core concept of the Church model [24]. In this thesis, we used the modified Church model that was derived by Grishenkov et al. [9] to identify the mechanical parameters of the magnetic-shelled microbubble. The mechanical parameters, such as the elasticity and viscosity, of the NEM are identified by linearizing the NEM similar to a forced harmonic oscillator and comparing with acoustic attenuation coefficient measurements. These mechanical parameters will further used in NEM for predicting UCA behaviors at different pressures and frequencies and with different pulse sequences.

3.6 PVA-MBs

Polyvinyl alcohol (PVA) is a water soluble, biodegradable, and biocompatible synthetic polymer [49]. PVA is mostly used in the paper and textile industries but also has several biomedical applications, especially in the field of tissue engineering [49]. In 2005, Cavalieri et al. [50] produced PVA-shelled MBs (see Figure 9). Here, the PVA shell was the result of the rearrangement of telechelic PVA molecules in the cross-linking network at the

air/water interphase. In the cross-linked PVA network, the hydroxyl (OH) group is a hydrophobic, i.e., water-loving, molecule and methane (CH2) is a hydrophilic, i.e., water resistant, molecule, which are responsible for encapsulation. The size distribution of the PVA-MBs is very narrow relative to other types of MBs (see Figure 10).
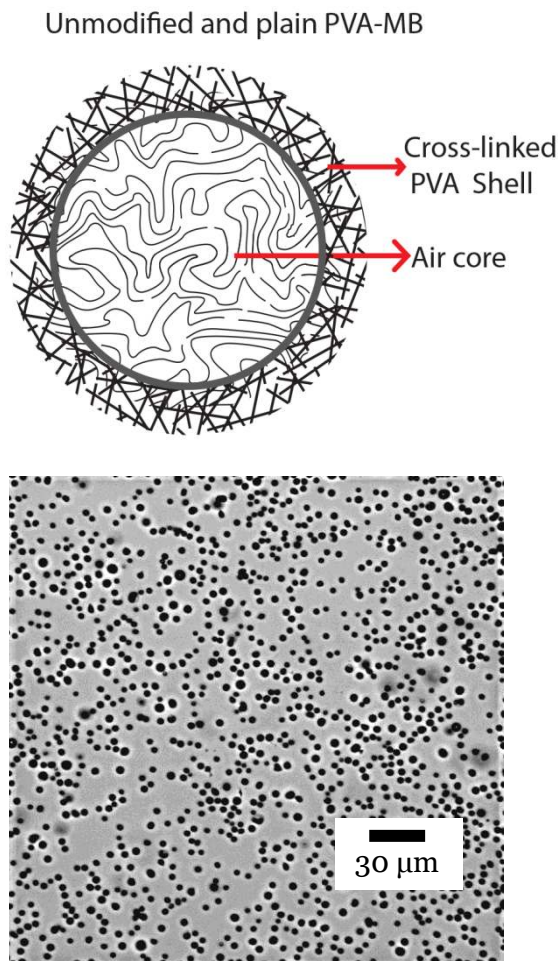
Figure 9. Schematic representation of PVA-shelled microbubbles. The outer layer is chemically modifiable to attach the targeted molecules, and the large shell thickness allows the loading of more significant amounts of nanoparticles in the shell.
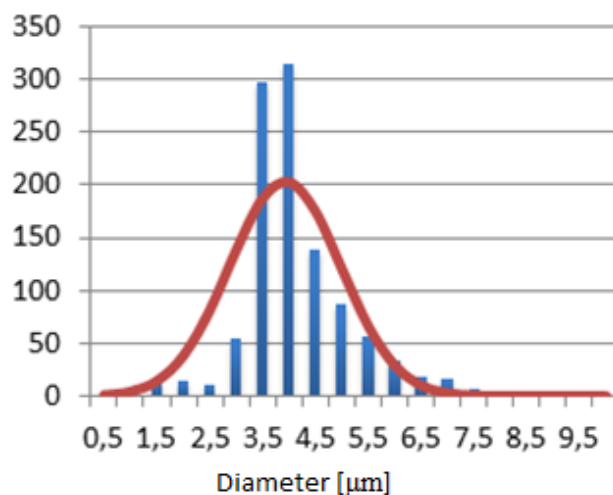
Figure 10. Optical micrograph of PVA-MBs dispersed in water with the corresponding size distribution.

The shell thickness of these MBs was identified to be between 200-800 nm (note: the variation in the shell thickness is because different techniques were used to obtain values) [9, 51]. Thus, the shell thickness is several times larger than in thin-shelled MBs, which are typically on the nm scale. The OH group on the MB surface is utilized to anchors the short peptides for promoting the integrin targeting of endothelial cells [11] and modified with the chitosan-galactosylated for delivering the doxorubicin to hepatocarcinoma cells [52]. Further, the PVA-MBs were thoroughly characterized in terms of acoustical responses [9, 10, 53], cytotoxicity [54], biocompatibility [11], and possibility to carry the therapeutic gases such as nitric oxide (NO) [55, 56].

3.7 Acoustophoresis

Ultrasound waves not only progress through matter but they can also induce an acoustic radiation force that causes particles displacement [57]. A century ago, the acoustic

radiation force acting on particles suspended in a liquid media, and their motion under acoustic waves was explored [58]. In the past two decades, several medical applications were identified based on the acoustic radiation force. For example, the acoustic radiation force is used to enhance the targeting efficiency of drug-loaded MBs [59].

In addition to the applications of the radiation force generated by a pulsed or continuous acoustic wave, the application of the radiation force on an acoustic standing-wave field is one of the fast-emerging area in the field of the precise non-handling manipulation or separation of cells/particles, concentration, sedimentation, sorting, and purification applications [60, 61]. For example, lipid particles from blood cells were successfully separated for lipid-free blood in cardiac surgery [62]. The standing-wave or stationary sound wave pattern has minima (nodes) and maxima (antinodes) that are obtained as the result of the superposition of two waves in opposite phases (see Figure 11).
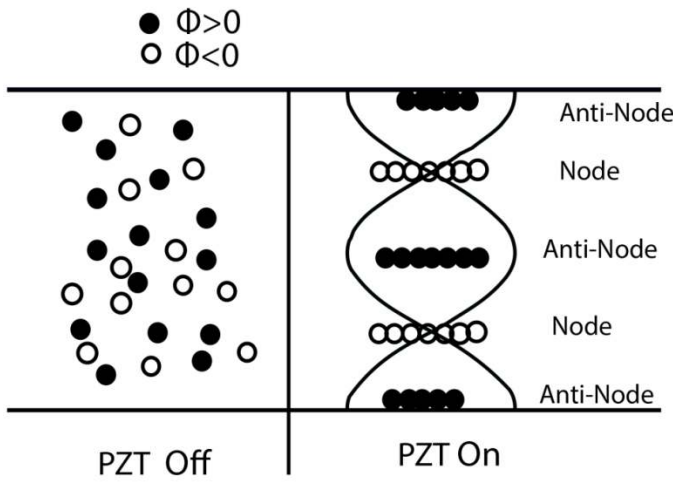
Figure 11. Illustration of the acoustic pressure standing wave profile and particle motion having different acoustic contrast factors, Φ, in a liquid suspension.

The primary radiation force drives particles to either a pressure node (velocity antinode) or a pressure antinode (velocity node), depending on the mechanical properties of the particles, such as density and compressibility. The mathematical representation of the primary radiation force [63] is given in Eq. 4,

$$F_y^{rad} = -\left(\frac{\pi p_a^2 V \beta_s}{\lambda}\right)\Phi(\beta, \rho)\sin(ky) , \tag{4}$$

where $k(=2\pi/\lambda)$ is the wavenumber, λ is the wavelength, y is the distance from the pressure node, p_a is the pressure amplitude, V is the volume of the particle and $\Phi(\beta, \rho)$ is the acoustic contrast factor, which is equal to $\frac{1}{3}f_1 + \frac{1}{2}f_2$. The monopole scattering coefficient, $f_1 = 1 - \frac{\beta_p}{\beta_s}$, and the dipole scattering coefficient, $f_2 = \frac{2(\rho_p - \rho_s)}{2\rho_p + \rho_s}$. The direction of particle movement depends on the sign of the acoustic contrast factor, Φ. Particles are translated and focused at the pressure node for Φ>0. Otherwise, the particles move in the opposite direction and are trapped at the pressure antinodes (see Figure. 11). The secondary radiation forces are responsible for attraction or repulsion between the particles [64].

4. METHODOLOGY

In this section, the methods that are used to study the objectives of the thesis, i.e., acoustic, mechanical, and physical properties of both unmodified, plain PVA-MBs and modified magnetized PVA-MBs, are described.

4.1. Scientific Methodology

The scientific methodologies employed to study each objective described in Chapter 2 are illustrated in Figure. 12. Previous knowledge of PVA-MBs has been included in the background section. Based on this prior knowledge, we formulated the following four research questions:

(1) Do the acoustical responses of modified PVA-MBs vary from that of unmodified PVA-MBs?

(2) Do the modified PVA-MBs alter the mechanical parameters compared to unmodified PVA-MBs?

(3) Does the direct visualization of the radial oscillation or fracturing mechanism of PVA-MBs correlate with the fracture mechanism of PVA-MBs obtained from backscattered time domain signals?

(4) Can we use the acoustophoresis method to manipulate and separate the PVA-MBs from solid polymer beads (resembling blood cells)?

Figure 12. Overview of the scientific methodology employed in this thesis.

Based on these research questions, we designed an experimental or a theoretical approach and observed results and validated simulations, leading to conclusions about the outcomes as follows:
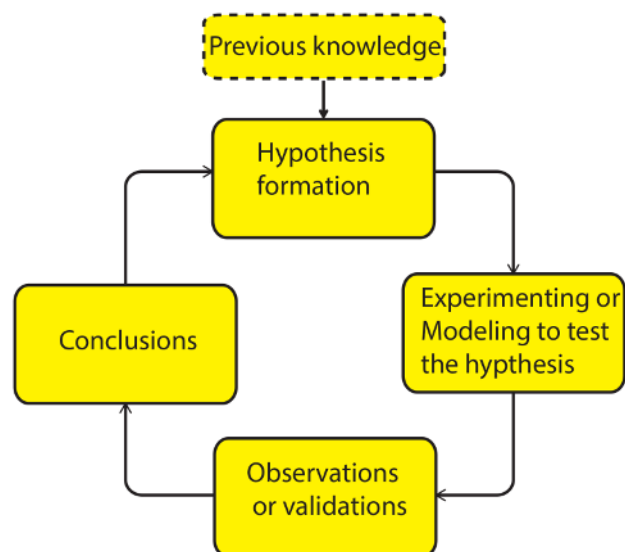
(I)   We developed an experimental setup to investigate the acoustical properties (such as the backscattered power and absorption at different frequencies and dilution rates and the fracture pressure threshold at different pressures) of modified PVA-MBs. The results of these experimental observations were validated by other techniques such as ultrasound imaging, MRI analysis, and crystallinity examinations (which were used in Papers 1 and 2).

(II)   We modeled the acoustic attenuation coefficient and phase velocity spectra and compared the results with experimental data. This comparison allows the estimation of mechanical parameters such as the shear modulus and loss modulus (described in Papers 3 and 4). Moreover, the outcome of the study is compared with atomic force microscopy (AFM) measurements.

(III)   We used a Brandaris-128 camera coupled with an ultrasound probe to visualize a single PVA-MB radial oscillation, and the results of the study were correlated with the backscattered time domain signals at high pressures (Paper 5).

(IV)   To test the PVA-MB motion caused by the radiation force in an acoustic standing-wave field, we used a piezoelectric transducer (PZT) coupled to a microfluidic chip that facilitates an ultrasound standing wave in a micro-chamber. The experimental results have been validated against theoretical calculations and previous studies.

After every study, new sub research questions are raised, which are described in the future work (Chapter 8).

4.2 Bubble preparation

4.2.1 PVA-MBs

PVA-MBs were produced in our lab according to the protocol described by Cavalieri et al. [50]. The powder form of PVA (Sigma-Aldrich, Chemie GmbH, Germany) was diluted in water and oxidized with sodium (meta)periodate, where the polymer chains were tailored to single moieties. This solution was then subjected to high shear stirring using an Ultra-Turrax® (Ika, Germany) tool, and during the process, polymer moieties collected around the water/air interface. The polymer moieties connected to each other through cross-linking. After this process, the floating PVA-MBs were separated from the polymer debris through a series of washing steps (these home-made PVA-MBs were used in Papers 5 and 6).

4.2.2. Modified PVA-MBs

In this thesis, we used two novel types of multimodal contrast agents (in Papers 1, 2, 3, and 4), which are the result of the combination of PVA-shelled MBs and superparamagnetic iron oxide (Fe_3O_4) nanoparticles (SPIONs). These modified MBs were prepared at the Universita degli Studi di Roma Tor Vergata (UNITV). The conjugation of PVA-MBs and SPIONs was obtained in two strategies (see Figures. 13b and c): (1) SPIONs were attached on the PVA shell through the chemical conjugation method (named MBs-chem) and (2)

SPIONs were physically entrapped inside the PVA shell (named MBs-phys). The micrographs of the MB-chem, and the MB-phys in Figure. 13b and c, elucidating the SPIONs' inclusion into/onto the PVA shell.
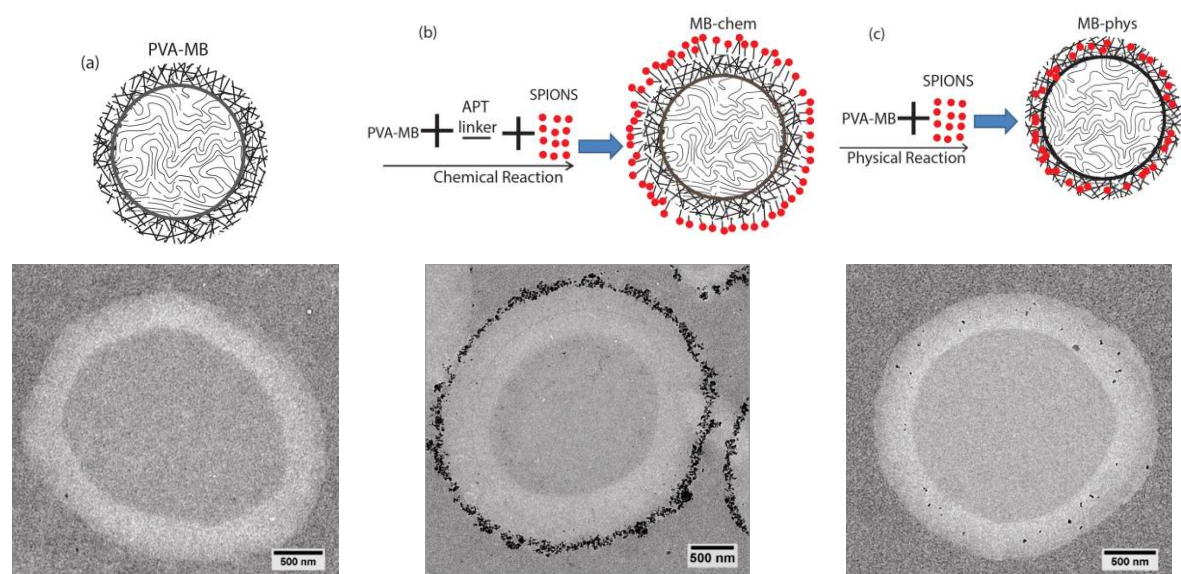
Figure 13. Schematic representation (top panel) and micrographs (bottom panel) of (a) plain PVA-MB (b) SPIONs (appeared as black dots) are attached on the PVA-MB (MB-chem), and (c) SPIONs are entrapped inside PVA-MB (MB-phys). The micrographic images are used here with the permission of Johan Härmark from the Department of Structural Biotechnology, KTH.

4.3 Structural Characterization

The amounts of SPIONs in MBs-chem and MBs-phys were found to be 29 %w/w and 15 %w/w, respectively. The assessment of SPIONs in the PVA shell was performed by thermogravimetric analysis (TGA) at the UNITV. The diameter and shell thickness (which are used in Paper 2) of both the modified MBs were obtained by atomic force microscope (AFM) measurements. These measurements were performed at the University of Bayreuth (UBT). The diameters of the MBs were obtained by a confocal laser microscope (CLM), and the shell thicknesses of the MBs were obtained by a transmission electron microscope (TEM), and these values were used for simulations in Paper 3. The confocal measurements were performed at the UNITV, and the TEM measurements were carried out at KTH.

Table 1. Average diameter, shell thickness, and iron content of particles obtained from TEM and AFM techniques.

Diameter and the shell thickness values from AFM measurements, used in Paper 2.				Diameter and shell thickness values from confocal microscopy and TEM measurements, considered in Paper 3.	
MB name	PVA-shelled MBs	MB-chem	MB-phys	MB-chem	MB-phys
Diameter [µm]	3.6±1.3	3.6±1.3	3.6±1.3	3.8±0.6	3.8±0.6
Shell thickness [nm]	215±133	215±133	215±133	315±44	415±54

4.4 Acoustic Characterization

In the acoustic characterization of MBs, the measurements were performed at different acoustic pressures and depend on the MBs radial oscillation the measurements classified into two pressure regimes as linear and nonlinear. These measurements are used to realize study objectives 1 and 2.

4.4.1 Linear regime

In the linear regime, MBs were excited with an incidental pressure of <100 kPa. The measurements include: (1) Backscattering power (BSP) (describes the intensity of the scattered signals from the MBs) and (2) absorption, which provides the acoustic wave attenuation (decrease in amplitude) and dispersion (phase velocity) information. All of these measurements were carried out at a temperature of 24±1°C and in different dilutions (concentrations) of MBs.
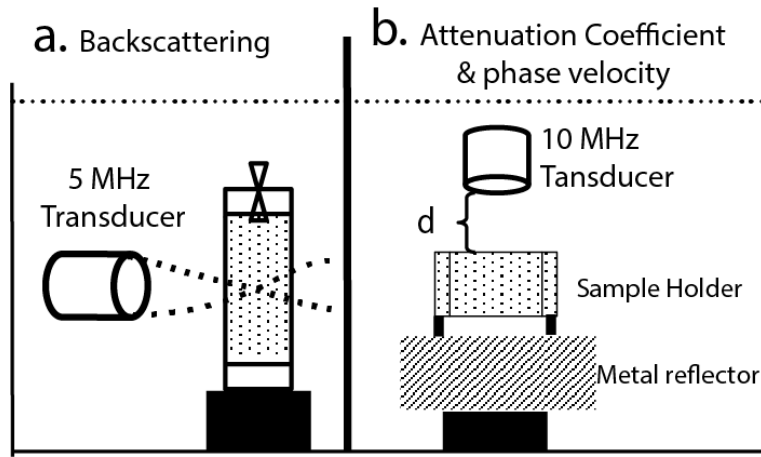
Figure 14. Schematic representation of experimental set-ups for measuring (a) the backscattering power and (b) the attenuation coefficient and the phase velocity spectra of PVA-MBs.

In the BSP measurements, the MB suspension was excited with a focused ultrasound transducer (5 MHz; Panametrics, V309, Waltham, MA, USA) and received by the same transducer (see Figure. 14a). For the attenuation coefficient and phase velocity measurements, a flat ultrasound transducer (10 MHz; Panametrics V311, Waltham, MA, USA) was used to acquire the back scattered signals from a metal reflector placed beneath the MB suspension (see Figure. 14b). In both experimental methods, the backscattered signals from a de-ionized and degassed water suspension (without MBs) were used as a reference signal to remove the noise and identify the actual signals from the MBs. Thus, reducing the scattered power of the MBs, P_{MB}, by the scattered power of the water, P_{ref}, gives the actual BSP of the MBs, which is given in Eq. 5,

$$BSP_{MB} = 10\log_{10}\left(\frac{P_{MB}}{P_{ref}}\right).$$

(5)

The mathematical representation of the attenuation coefficient and phase velocity of the MB suspension is given in Eq. 6 and 7,

$$\alpha(\omega) = -\frac{1}{2L}\left(\frac{|F_{MB}(\omega,L)|}{|F_{ref}(\omega,L)|}\right)\text{Np/cm} \quad \text{(or)} \quad \alpha(\omega) = -\frac{20}{2L}\log\left(\frac{|F_{MB}(\omega,L)|}{|F_{ref}(\omega,L)|}\right)\text{dB/cm,} \qquad (6)$$

$$\frac{1}{c_{MB}(\omega)} = \frac{1}{c_{ref}} - \left[\frac{\phi(F_{MB}(\omega,L)) - \phi(F_{ref}(\omega,L))}{2L\omega}\right] \text{(m/s).} \qquad (7)$$

The terms $|F_{MB}(\omega)|$, $|F_{water}(\omega)|$, ϕ_{MB}, and ϕ_{water} are the magnitudes and phases of the retrieved signals from the MB suspension and water, respectively. The speed of sound in pure water, c_{ref}, at the room temperature of 24°C is approximately 1494 m/s. The detailed derivation is given in the appended Paper 3.

4.4.2 Nonlinear regime

In the nonlinear regime, the MBs were excited at an incidental pressure between 0.1 MPa and 2.5 MPa. Two experimental set-ups one is pure acoustical setup were used to assess the fracturing mechanism.

Acoustical Assessment

In the acoustic assessment method, a bulk suspension of PVA-MBs was introduced in a custom-made cylindrical agar phantom. The MB suspension in the agar phantom was excited by a focused ultrasound transducer (Gamma Series; Krautkramer Inc., Lewistown, PA; 2.2 MHz), and the backscattered time domain signals were detected by another focused ultrasound transducer (Panametrics, V309, Waltham, MA; 5 MHz) (see Figure. 15). The excitation pulses consist of different pressure amplitudes varied between 0.4-2.5 MPa. On each excitation, approximately 100 time-domain signals were acquired.
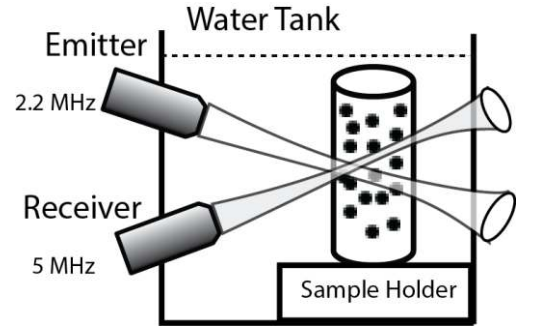
Figure 15. Schematic illustration of the acoustic set-up.

In the study of the ultrasound-induced fracture mechanism, the peak-to-peak amplitudes of backscattered signals from PVA-MB suspension at high insonation bursts at a pressure of approximately 1 MPa were considered. Also power spectra of these backscattered-time domain signals were constructed to investigate the acoustic emission patterns (in Paper 5).

Fracture pressure threshold

The fracture pressure threshold of the MBs describes the threshold between the nonlinear oscillations and disruption. Here, the MB fracturing events were estimated based on the evaluation of the change of shape of the time-domain acoustic signals acquired from consecutive insonation pulses. For example, the backscattered time-domain signals of a MB suspension at low pressure are almost similar (see Figure. 16a), and at high pressures, they are evidently different from each other (see Figure. 16b).
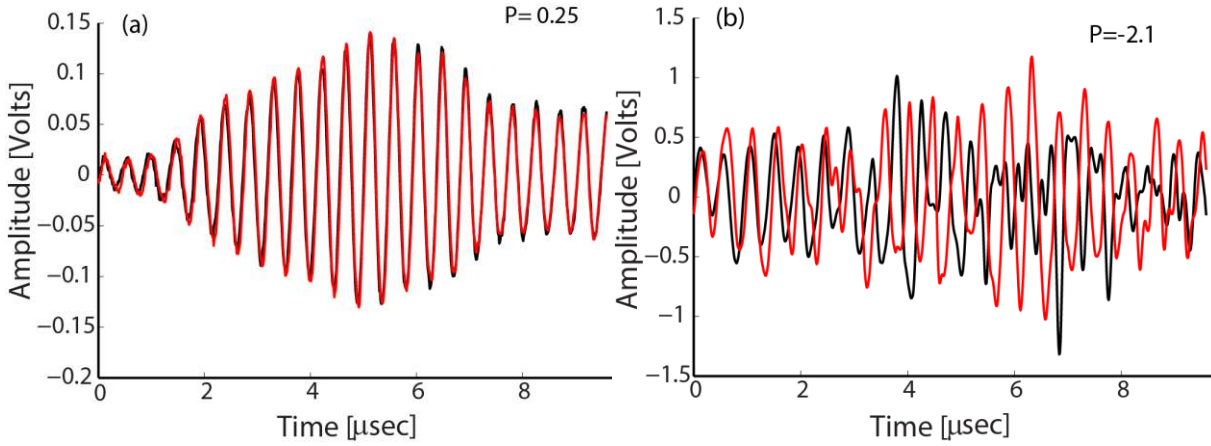
Figure 16. Two consecutive backscattered time domain signals (illustrated as solid line and dot line) obtained from the PVA-MB suspension (a) at a low acoustic pressure of approximately 0.25 MPa and (b) at a high pressure of approximately 2.1 MPa.
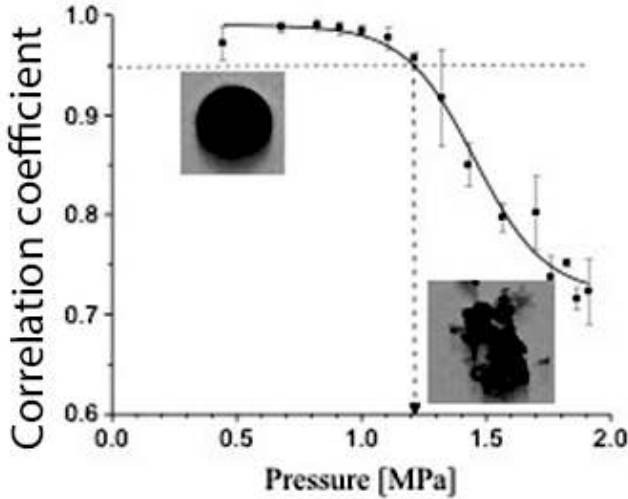
Figure 17. Maximum correlation coefficient, r vs. the peak negative pressure. The intersection between the best fit to the data and the threshold value of 0.95 determines the value of the fracture pressure threshold (P_{thr}). Enclosed plots: after insonification below P_{thr}, regular spherical MBs were detected (left); after insonification above P_{thr}, irregular large fragments of the shell were observed (right).

To determine the change in the shape of consecutive pulses, we used the cross-correlation technique (given in Eq. 8).

$$\max\left|\rho\left(\tau|T\right)\right| = \max\left|\frac{\int f\left(t|T\right)f\left(t-\tau|T+\Delta T\right)dt}{\left\{\left[\int f^2\left(t|T\right)dt\right]\left[\int f^2\left(t|T+\Delta T\right)dt\right]\right\}^{1/2}}\right| \tag{8}$$

Parameter τ is the time lag; T and $T+\Delta T$ are the times between two consecutive acquired signals; and $max|\rho(\tau|T)|$ is the maximum normalized correlation coefficient. The value of $max|\rho(\tau|T)|$ varies between '0' (indicating a weak relationship between data sets) and '1' (a very strong relationship between data sets). The mean value of $max|\rho(\tau|T)|$ equal to 0.95 was proposed as a fracturing threshold, P_{thr}, from which the peak negative pressure was estimated (see Figure 17). That means that if the MBs are excited below P_{thr}, then the radial oscillation of MBs in consecutive acquired time domain signals remains similar; if the MBs

are excited above P_{thr}, then the signal shape varies significantly between consecutively acquired time-domain signals. The data are fitted with the Boltzmann sigmoid function in Matlab®. From the fitting, the pressure fracture threshold, P_{thr} (at which the curve crosses below the 95% correlation coefficient) is identified (see Figure. 17).

Opto-acoustic assessment

In this method, a single PVA-MB was acoustically excited by a broadband focused ultrasound transducer (PA275, Precision Acoustics, Dorchester, UK; 1 to 9 MHz). An ultra-high-speed Brandaris-128 camera (see Figure. 18) was used to visualize the radial oscillation of the MB. Here, the MB was insonified with a pressure of approximately 1 MPa.
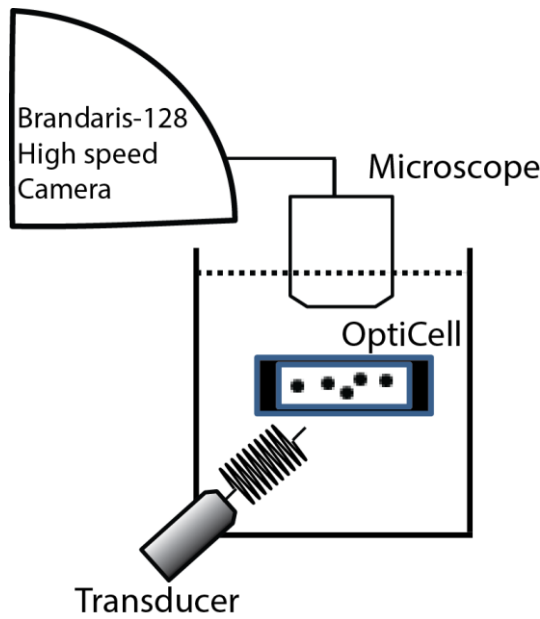
Figure 18. Schematic illustration of an opto-acoustic experimental setup, including the ultra-high-speed Brandaris-128 optical camera coupled to the transducer.

The frequencies of the excitations varied between 2-4 MHz in intervals of 0.2 MHz (16 pulses), with a pulse repetition frequency (PRF) of 10 Hz. For each PVA-MB, a series of 17 clips of 128 frames was captured by the Brandaris-128 camera at a rate of 15 million frames per second. The first clip in each series was acquired without the application of ultrasound to estimate the initial radius of the MB. The following 16 clips revealed the dynamics of the MB in response to ultrasound exposure. As mentioned above, we captured a total of 11 individual PVA-MBs oscillation under each set of ultrasound parameters (P_{pk-} = 1 MPa; f = 2 to 4 MHz in 0.2 MHz increments). Thus, a total of 132 video clips were recorded and analyzed in Matlab® (The Math-Works Inc., Natick, MA).

4.5 Modeling

The viscoelastic properties of the encapsulated shell also played an important role in understanding the acoustical behavior of the MBs upon the ultrasound exposure. In this thesis, the viscoelastic properties of the shell were retrieved by comparing the attenuation coefficient and phase velocity measurements with the linearized theoretical model. The attenuation coefficient can be obtained using either the extinction cross-section, σ_e, or the complex speed of sound in the bubbly liquid, c_m [15].

4.5.1 Extinction cross section

The extinction cross-section, σ_e, is the sum of the σ_s (mentioned in the background chapter) and the absorption cross-section, σ_a, and it can also mathematically expressed in terms of damping as given in Eq. 9,

$$\sigma_e = \sigma_S \frac{\delta_{tot}}{\delta_C} = 4\pi R_{01}^2 \frac{\Omega^4}{\left(1-\Omega^2\right)^2 + \left(\Omega\delta_{tot}\right)^2} \frac{\delta_{tot}}{\delta_C}, \tag{9}$$

where $\omega(=2\pi f)$ is the radial driving frequency, δ_{tot} is the total damping coefficient which is the sum of four damping parameters: thermal damping δ_{th}, radiation damping δ_c, liquid viscosity δ_L, and shell viscosity δ_S. The δ_{th} and δ_{th} mathematical representation are given in Eq. 10 and 11, $\Omega(=\omega/\omega_0)$ is the normalized frequency and R_{01} is the inner radius of the MB at rest.

$$\delta_c = \frac{\omega^2 R_{02}}{c}\left[1+\left(\frac{\omega R_{02}}{c}\right)^2\right]^{-1}, \tag{10} \qquad \delta_{th} = \frac{3p_0}{\omega\rho_S R_{01}^2\alpha}\,\text{Im}\left(\frac{1}{\phi(R_{01},\omega)}\right). \tag{11}$$

Both δ_L and δ_S and also the radial resonance frequency, ω_o, are obtained from the linearized version of the nonlinear equation of motion. We used the linearized version of NEM, proposed by Grishenkov et al. [9]. Here the Fourier decomposition of the linearized version of NEM is given in Eq. 12,

$$\left[-\omega^2 + j\frac{4}{\alpha\rho_S R_{01}^2 R_{02}^3}\left(R_{01}^3\mu_L\omega + V_S G''(\omega)\right) + \frac{1}{\alpha\rho_S R_{01}^2}\left(3\kappa P_{G,eq} + \frac{4V_S}{R_{02}^3}G'(\omega)\right)\right]X(\omega)$$
$$= \frac{\Delta\hat{P}}{\alpha\rho_S R_{01}^2}, \tag{12}$$

$$\text{where } \alpha = \left[1+\left(\frac{\rho_L - \rho_S}{\rho_S}\right)\frac{R_{01}}{R_{02}}\right].$$

By comparing Eq. 12 with the Eq. 13 for the damped harmonic oscillator (consisting of a dashpot, a spring, and a mass system as shown in Figure. 19), we can identify ζ_S and ζ_L (as given in Eq. 14 and 15), and resonance frequency, ω_o (given in Eq. 16),

$$\left(-\omega^2 + j\delta\omega\omega_0 + \omega_0^2\right)X(\omega) = \frac{\Delta\hat{P}}{\alpha\rho_S R_{01}^2} \tag{13}$$
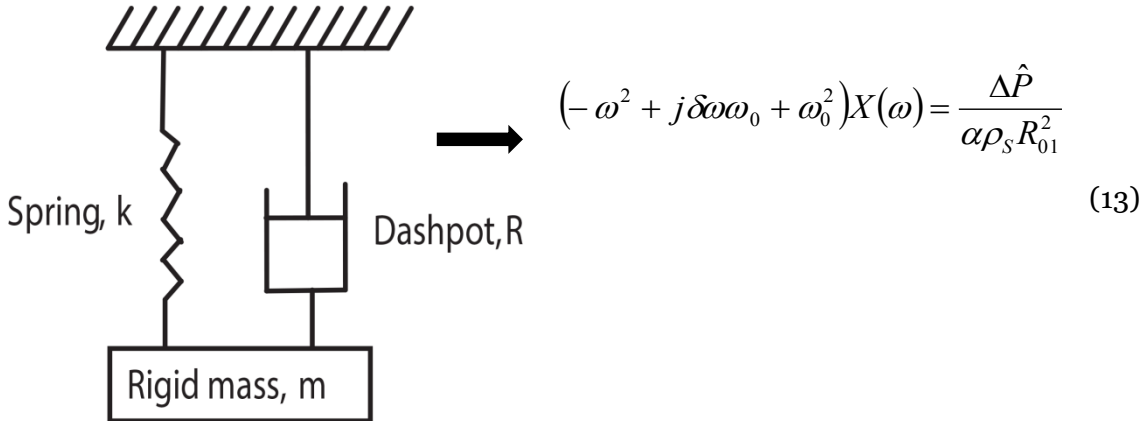
Figure 19. Illustration of a simple damping mechanical oscillator

$$\delta_S = \frac{4V_S G''(\omega)}{\alpha\omega_0\rho_S R_{01}^2 R_{02}^3} \qquad \delta_L = \frac{4R_{01}^3\mu_L}{\alpha\omega_0\rho_S R_{01}^2 R_{02}^3} \qquad \omega_0 = \sqrt{\frac{1}{\alpha\rho_S R_{01}^2}\left(3\kappa P_{G,eq} + \frac{4V_S}{R_{02}^3}G'(\omega)\right)}$$

$$(14), \qquad\qquad (15), \qquad\qquad (16).$$

$G'(\omega)$ and $G''(\omega)$ are the frequency dependent storage modulus and loss modulus, which are expressed as: $G'(\omega) = G_{eq} + G_1\omega^{3/4}$ and $G''(\omega) = \omega(\mu_0 - \mu_1\omega)$, respectively. Here, G_{eq} and μ_{eq} are the equilibrium shear modulus and shear viscosity, whereas G_1 and μ_1 are the frequency dependent complex shear modulus and shear viscosity, respectively.

The mathematical expression for the attenuation coefficient, $\alpha(\omega)$, is given in Eq. 17,

$$\alpha(\omega) = 10\log e \int_0^\infty \sigma_e(R_{01},\omega)n(R_{01})dR_{01}. \tag{17}$$

The above formula was used in Paper 3 to retrieve the viscoelastic properties of the modified and unmodified PVA-MBs at different dilution rates. The four unknown variables G_{eq}, μ_{eq}, G_1, and μ_1 were identified from the best fit between the measured acoustic attenuation coefficient data and the theoretically estimated attenuation coefficient. The choice of simulation parameters is listed in Table 2.

Table 2. Values of parameters used in the simulations

Parameter	Value
Liquid density, ρ_L	1000 kg/m³
Shell density, ρ_S	1054 kg/m³ for PVA-MBs
	1774 kg/m³ for MB-chem
	1393 kg/m³ for MB-phys
Liquid viscosity, μ_L	1×10⁻³ Pa.s
Ambient pressure, p_o	0.1 MPa

4.5.2 Complex speed of sound in a bubbly liquid

In Paper 3, the four unknown variables (G_{eq}, G_1, μ_{eq}, and μ_1,) were estimated by solving one data (acoustic attenuation coefficient) set, which is not the best scenario. For more corroboration, we employed the reconstruction of both the attenuation spectra and phase velocity spectra from the same time domain data (used in Paper 3). In general, the phase contains more structural information than the attenuation coefficient data [65]. A simultaneous fit of these two curves with one unique set of viscoelastic parameters brings additional confidence to the overall modeling results.

The simultaneous spectra of the attenuation coefficient and phase velocity were achieved using the c_c expression, which is given in Eq. 18,

$$c_c = \frac{c_{ref}}{\sqrt{1 + \dfrac{4\pi c_{ref}^2 \rho_L}{\alpha \rho_S} \displaystyle\int_{R_1}^{R_n} \dfrac{R}{\omega_0^2 - \omega^2 + 2j\zeta_{tot}\omega\omega_0} n(R)dR}}, \tag{18}$$

where $n(R)dR$ is the number of bubbles per unit volume within the radius of $(R, R+dR)$, c_{ref} is the speed of sound surround media, $\omega_0(=2\pi f_0)$ is the radial resonance frequency, and ζ_{tot} is the total damping ratio, which is equal to the total damping coefficient, $\zeta_{tot} = \delta_{tot}/2$.

4.5.2 Statistical evaluation

In Paper-III, during the curve-fitting process, both the mean square error (MSE) and the correlation coefficient (R_{coeff}) were used to assess the goodness of fit. In each fitting process, several combinations of R_{coeff} and MSE are obtained. The R_{coeff} values vary from 0 to 1, with an R_{coeff} value of '1' indicating a strong linear relationship between data sets. MSE values vary from 0 to ∞, with an MSE value of '0' representing an ideal fit between data sets. Therefore, a combination of maximum R_{coeff} and minimum MSE values is required to identify the best possible agreement between the experiments and theory. The best combination of the maximum R_{coeff} - minimum MSE is identified with the assistance of a rank-based decision-combination method. In the rank-based algorithm, R_{coeff} and MSE non-metric data were classified into two data sets, and then the data sets are weighted with integer values (from 0 to N). The rank vectors r_{Ri} and r_{MSEi} were further combined and the minimum value of $r_{Ri}+r_{MSEi}$ was found, which corresponds to the best combination of a maximum R_{coeff} - minimum MSE and at this value the best fit was found. The best fit further accompanied with the 95% confidential intervals.

4.6 Acoustophoresis

Acoustophoresis addresses the particle manipulation or separation using the ultrasound standing wave (USW). We chose a microfluidic chip (GeSim GmbH, Dresden, Germany) consisting of a rectangular chamber coupled to a PZT. The frequency of the PZT was chosen to be 2.8 MHz (wavelength =535 µm), which equals the width of the rectangular chamber, to create a USW (see Figure. 20).
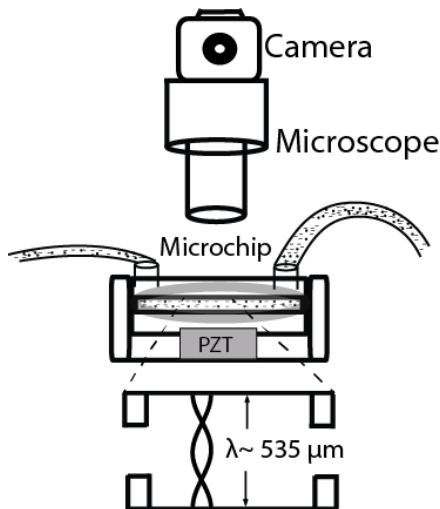
Figure 20. Schematic representation of the experimental setup that consists of a silicon/glass microchip connected to a PZT transducer mounted under a microscopy and a CCD camera. Zoomed-in frame demonstrates the standing wave profile in rectangular chamber.

A transmission microscope (Axiovert 40 CFL, Carl Zeiss, USA) equipped with a 10x object lens (NA= 0.25; Zeiss, Germany) was focused on the rectangular chamber. The scattered light from chamber was captured by a digital camera (SLT–A77V, 77α, Minato, Japan) with a frame rate of 50 Hz. The experiments were performed in the non-flow condition, in which the particles were at rest. The electrical potential across the PZT (which is indirectly proportional to the pressure generated in the microfluidic chip) was incrementally increased between 1 and 10 volts. The motion of the particles was recorded for approximately two minutes at each voltage and further their motion evaluated in Matlab®.

5. RESULTS

This chapter presents an overview of the main results achieved during the presented thesis work. All of the results are described in detail in the appended Papers 1 to 6.

5.1 Acoustic Characterization

In this section, the summarized results of the acoustical examinations are presented. These results are adopted from Papers 1 and 2, and the results are related to object 1.

5.1.1 Backscattering power, attenuation coefficient and phase velocity

The average maximum BSP, attenuation coefficient, and phase velocity values of MBs-chem and MBs-phys at the driving frequencies for different dilutions are presented in Figure. 21. Evidently, for a fixed MB concentration (below 10^6 MBs/ml), MBs-chem yields more efficient backscattering than MBs-phys. The BSP of MBs-chem linearly increases with the concentration until it reaches 4.4×10^5 MBs/ml (where the maximum BSP of 20 dB is achieved), and it decreases above this concentration. On the other hand, a maximum BSP of MBs-phys of approximately 20 dB is obtained at a concentration of 2.0×10^6 MBs/ml, and above this concentration, the BSP is saturated.
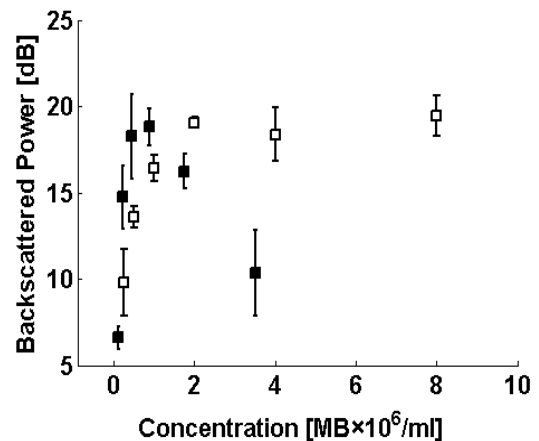
Figure 21. Maximum backscattering power vs. concentration of MBs with chemically bound SPIONs, MBs-chem (■) and embedded SPIONs, MBs-phys (□).

The attenuation coefficient values increase and the phase velocity values decrease linearly as the number of MBs increase in the insonified volume. The maximum attenuation coefficient is approximately 20 dB, observed at a concentration of 1.8×10^6 MBs/ml for MBs-chem and a concentration of 8.0×10^6 MBs/ml for MBs-phys. The phase velocity values at lower concentrations reach the speed of sound in pure water at 24°C, whereas the phase velocity at high concentrations is almost 25 m/s lower than the speed of sound.
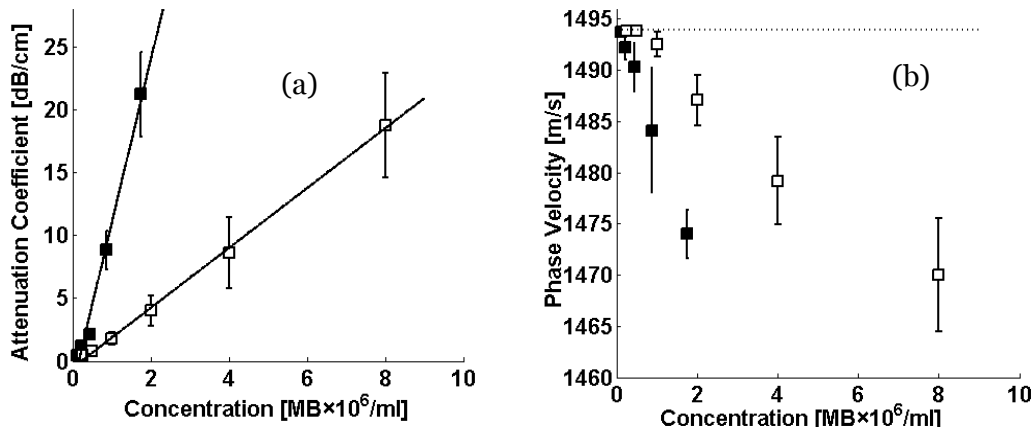
Figure 22. Maximum (a) attenuation coefficient and (b) phase velocity vs. concentration of MBs with chemically bound SPIONs, MBs-chem (■) and embedded SPIONs, MBs-phys (□). The dashed line in (b) represents the value of the speed of sound at 24°C.

5.1.2 Fracturing threshold

The correlation coefficients, R_{coeff}, of the consecutive backscattered signals acquired from the MB-chem and MB-phys suspensions with respect to the acoustic pressures (varies between 0.2-2.2 MPa) are presented in Figure. 23. The data are fitted with the Boltzmann sigmoid function and from the fitting, the pressure fracture threshold, P_{thr}, (at which the curve crosses below the 95% correlation coefficient) is identified (see Figure. 23). Here the R_{coeff} data are obtained when the insonation pulse consists of 12 cycles.
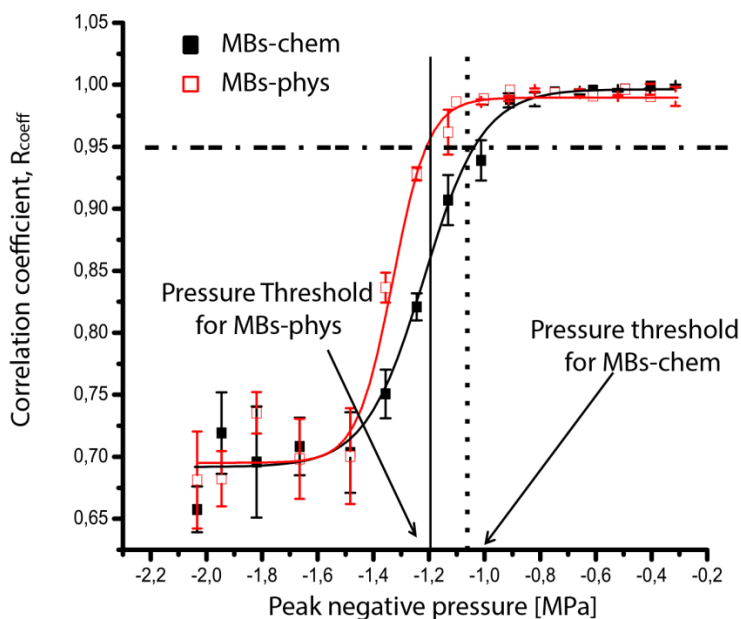
Figure 23. Correlation coefficient data of the consecutive backscattered signals acquired from the insonified MBs-chem (red dots) and MBs-phys (black dots) suspensions at different pressures. The data are compared and fitted with the Boltzmann sigmoid function (red line for MBs-chem and black line for MBs-phys). From the curve fitting, the P_{thr} is identified.

Further, the P_{thr} of both MBs-chem and MBs-phys are found with respect to the insonation pulse, consisting of numbers of cycles of 10, 8, and 6 (see Figure. 24). The P_{thr} of MB-chem decreases as the number of cycles in the pulse, N, increases. On the other hand, the P_{thr} of MBs-phys at N= 8, 10 and 12 cycles shows approximately the same value of the fracturing pressure threshold, P_{thr}, approximately 1.2 MPa. The P_{thr} of MBs-chem is lower than (except at N=8) the P_{thr} of MBs-phys.
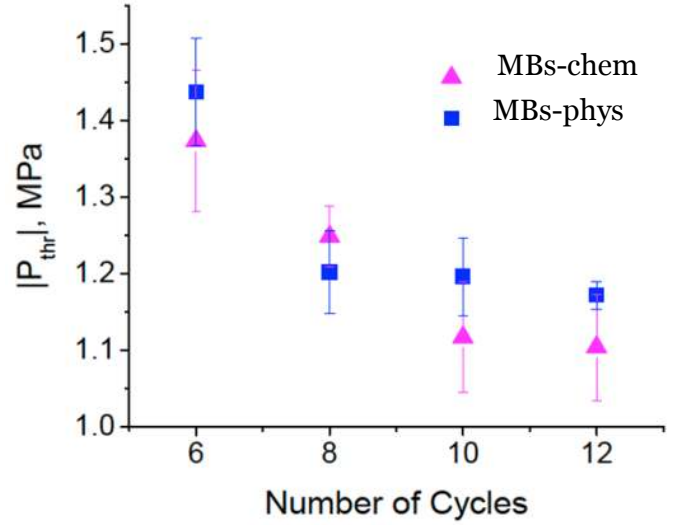
Figure 24. The absolute value of P_{thr} vs. number of cycles for MBs-chem and MBs-phys.

5.2 Modeling

In this section, the mechanical and physical properties of MBs-phys and MBs-chem are presented, as acquired from the fitting theoretical attenuation coefficient and phase velocity spectra with experimental results. The results of the fitting analysis are adopted from Papers 3 and 4, and they are part of the objective 2 study.

In Paper 3, the measured attenuation coefficient spectra are compared with the theoretically estimated attenuation coefficient spectra at high, moderate, and low concentrations of plain PVA-MBs, MBs-chem, and MBs-phys (see Figure. 25). The low, moderate, and high concentrations of PVA-MBs, MBs-chem, and MBs-phys are provided in Table 3. The corresponding unknown variables obtained from the best fittings are listed in Table 3. It is evident that the storage modulus, $G'(\omega)$ and loss modulus, $G''(\omega)$, of MBs-phys are significantly larger than those of MBs-chem and unmodified PVA-MBs.

In Paper 4, the unknown parameters (G_{eq}, G_1, μ_0, μ_1) and the resonance frequency, f_0, of MBs-chem and MBs-phys are acquired (listed in Table 4, at the driving frequency 10 MHz) by the simultaneous fitting of the attenuation coefficient and phase velocity spectra (see Figure. 26). The fittings are accompanied by the 95% confidence interval. The total damping ratios, ζ_{tot}, of the MBs-chem and MBs-phys surrounding liquid, radiation, and thermal damping are also determined. The damping ratios of e plain PVA-MBs and the lipid-shelled MB (Sonazoid™) are also plotted (see Figure. 27) for comparative purposes.
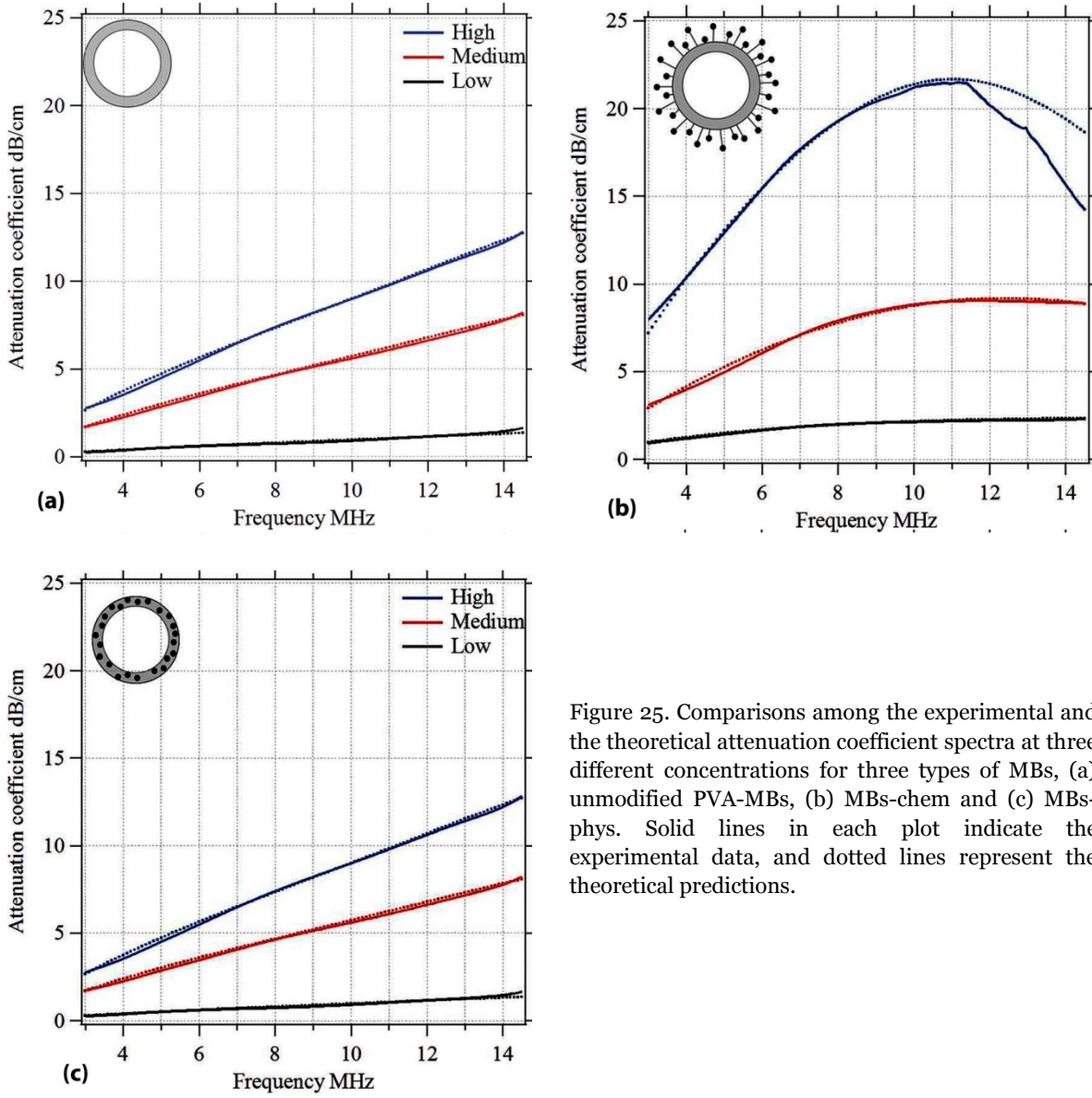
Figure 25. Comparisons among the experimental and the theoretical attenuation coefficient spectra at three different concentrations for three types of MBs, (a) unmodified PVA-MBs, (b) MBs-chem and (c) MBs-phys. Solid lines in each plot indicate the experimental data, and dotted lines represent the theoretical predictions.

Table 3. List of parameters used for modeling the frequency-dependent acoustic attenuation coefficients of modified and unmodified PVA-MBs. This table is adopted from Paper 3.

Parameter	Plain	MB-chem			MB-phys
Concentration, x10^6 [MB/ml]	0.2; 0.9; 1.8	0.4	0.9	2.0	0.5 ;1.0 ;2.0
G_{eq} [MPa]	10.5	4.0	3.8	4.0	28.0
G_1 [Pa/ (rad/s)$^{3/4}$]	5.5	10.7	4.2	0.1	10.0
μ_0 [Pa·s]	0.6	0.3	0.2	0.2	0.7
μ_1 x 10^{-9} [Pa·s^2/rad]	3.2	0.01	0.9	2.0	2.0
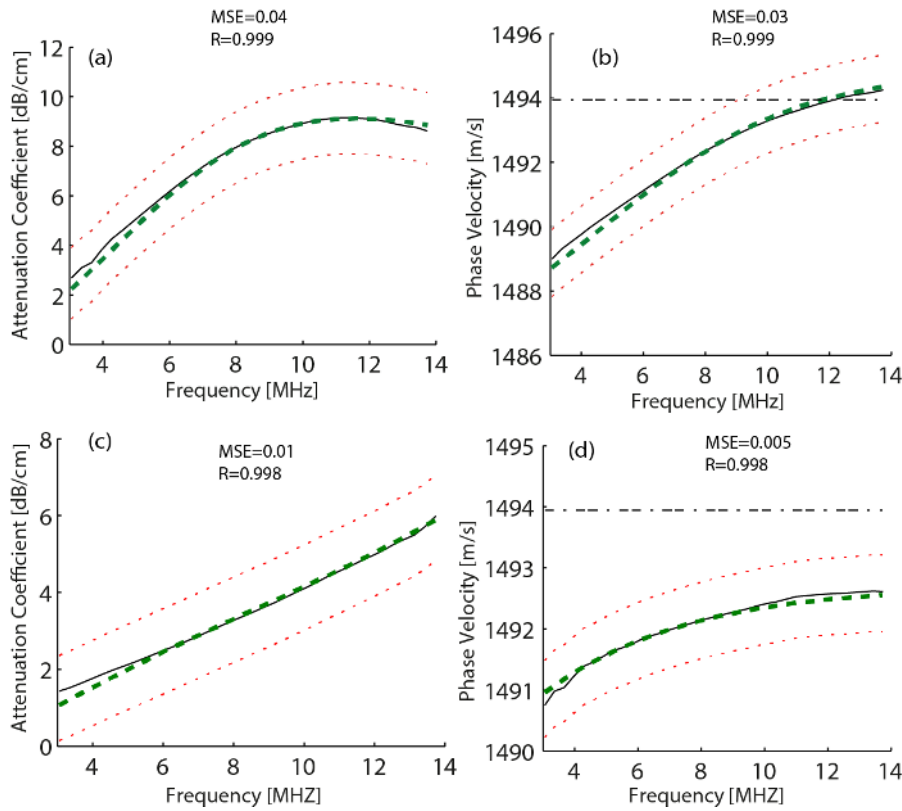
Figure 26. Comparison of experimental attenuation coefficient, phase velocity (solid black color) and theory (solid green color) with 95% CI (dashed red color): attenuation coefficient and phase velocity spectra of (a, b) MBs-chem (c, d) MBs-phys

Table 4. Four unknown viscoelastic coefficients G_{eq}, G_1, μ_{eq}, and μ_1 of MBs-chem and MBs-phys are estimated by modeling the ultrasound attenuation coefficient measurements.

Mechanical properties of MBs-chem, MBs-phys adopted from Paper 4							
Type of MB	Shell thickness [nm]	C [MB/ml]× 10^6	G_{eq} [MPa]	G_1 [Pa/ $(rad/s)^{3/4}$]	μ_{eq} [Pa·s]	$\mu_1 \times 10^9$ [Pa·s²/rad]	f_0 [MHZ]
MB-chem	315±44	0.88	9.5±1.0	1.9±1.3	0.3±0.02	0.4±0.2	13.4±2.2
MBs-phys	415±54	2.0	22.0±5.0	17.6±2.5	0.8±0.01	4.4±0.7	27.6±5.9

The total damping ratio, ζ_{tot}, values of all PVA-based MBs, plain PVA-MBs, MBs-chem and MBs-phys, are significantly higher that of Sonazoid™ MBs. The damping caused by the shell is the reason for the higher damping in PVA-based MBs. The shell damping decreases with an increase in the driving frequency, f, due to the terms G''/ω and $1/\omega_0$ (as given in Eq. 15). Different from the PVA-based MBs, the frequency-dependent radiation damping, ζ_c, increases significantly in Sonazoid™ UCA and starts to be comparable with the shell damping at approximately 10 MHz. As a result, the total damping increases with the frequency for Sonazoid™ UCA (see Figure. 27d).
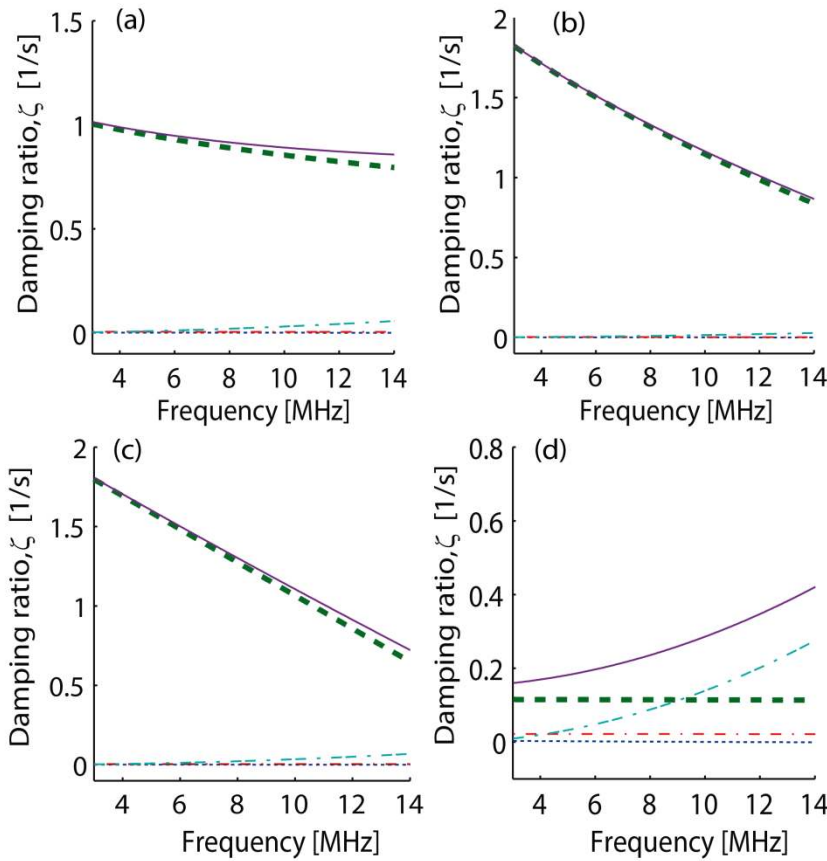
Figure 27. Total damping coefficient (solid), which is the sum of the thermal damping (dot), shell damping (dash), liquid damping (dash-dot) and radiation damping (dash-dash-dot) for (a) MBs-chem, (b) MBs-phys, (c) plain PVA-MBs and (d) lipid-shelled contrast agent Sonazoid™.

5.3 Nonlinear Oscillations

In this section, we present the radial oscillations of single PVA-MBs and backscattered time-domain signals and corresponding power spectra from a bulk PVA-MB suspension caused by the interaction of high-intensity ultrasound bursts. These results are adopted from Paper 5, and the following results are related to object 3.

5.3.1 Optical visualization

The radial excursions of the PVA-MBs upon a high-intensity ultrasound burst (pressure is approximately 1 MPa, and the nominal f is equal 2 MHz) are presented in 48 frames (frames 28 to 75) of 128 frames (see Figure. 28). The diameter of the MB at rest (in the 28th frame) is approximately 4.14 μm. The PVA-MB shell is buckled and compressed (see frames 29-33), recovers from the compression (frame 34), and expands (see in frames 35-36). The maximum expansion and compression of MB are identified to be approximately 4.83 μm and 2.3 μm, respectively, so it is evident that the PVA-MB exhibits more compression than expansion (see frames 48-50). The first crack is observed in frame 52, but there is no sign of gas leakage through the crack. In the later frames, the gas core of the MB is held back and retains its spherical shape. The number of crack sources multiplies with the insonation cycles (in frames 62 and 72).

The fractured shell holds a portion of the gas, and the resultant non-spherical fractured MB is still acoustically active upon consecutive insonation pulses (see Figure. 29). The

volume fraction of the gas core decreases as the MB is exposed to several consecutive bursts. This indicates that the gas is slowly pumped out through the pores. After all gas molecules are squeezed out of the PVA-MB, the PVA shell remains intact in the shape of a deflated ball (see last row in Figure. 29).
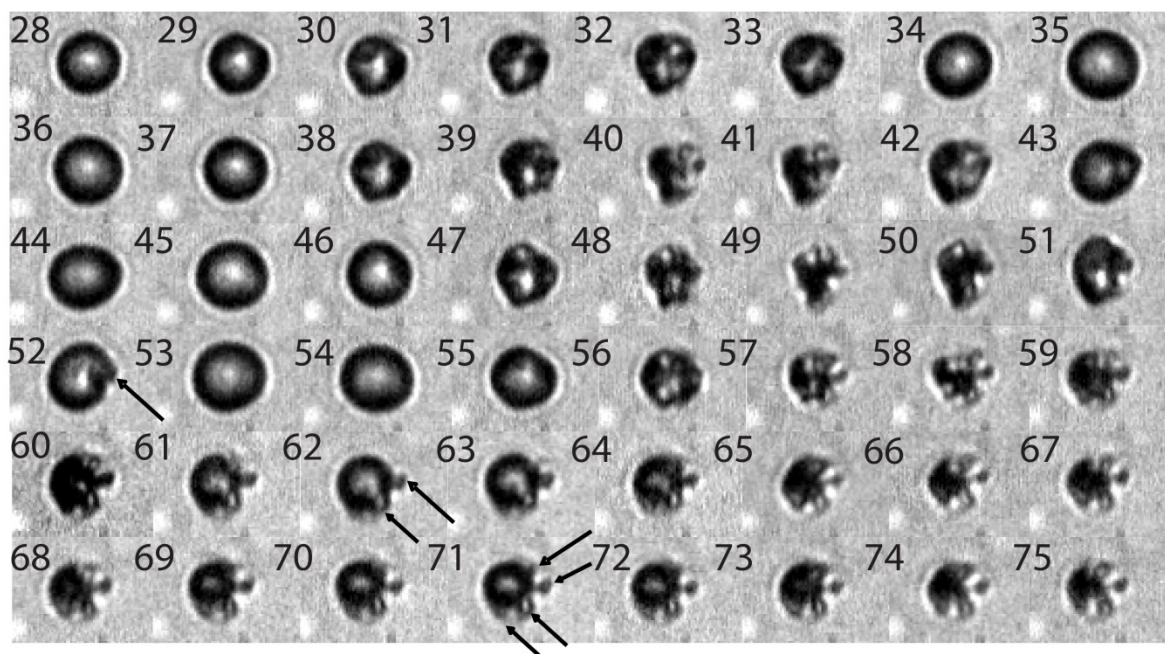
Figure 28. Sequence of 48 image frames of a 4.2 μm PVA-MB driven by ten cycles of an ultrasound burst at a 2 MHz frequency with a pressure of approximately 1 MPa.
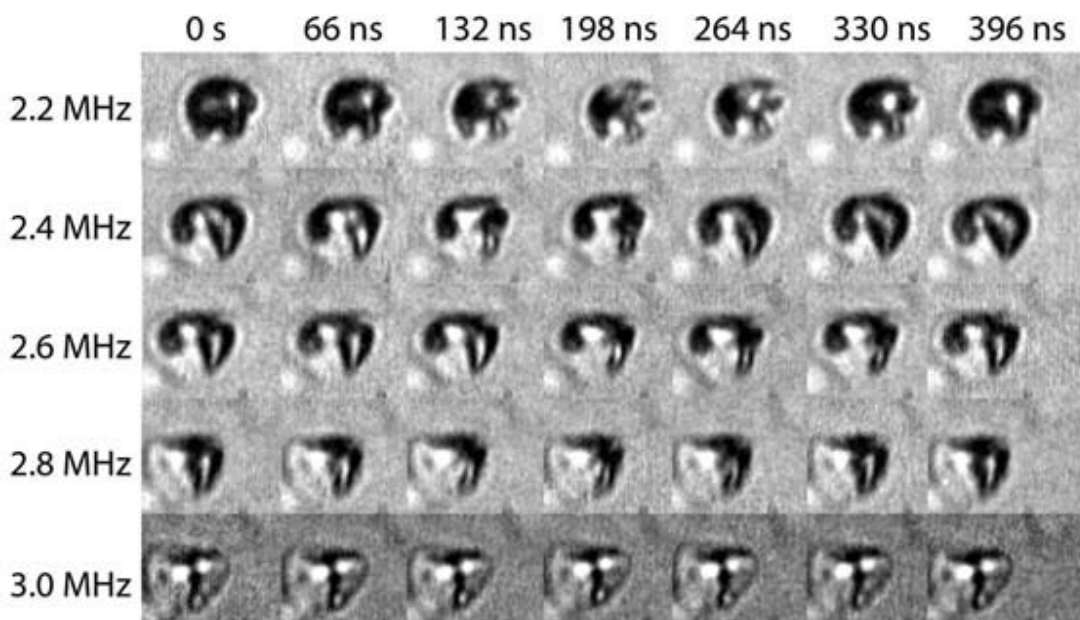
Figure 29. Sequence of 7 image frames of a broken PVA-MB at insonation frequencies of 2.2, 2.4, 2.6, 2.8, and 3.0 MHz.

5.3.2 Acoustical observations

The peak-to-peak amplitude, A_{pk-pk}, of the backscattered time-domain signals of the bulk PVA-MB suspension at 0.16 MPa (before dashed line) and 1 MPa (after dashed line) is presented in Figure. 30. The A_{pk-pk} values at 0.16 MPa are constant and exhibit a minor radial oscillation of MBs, in which only the fundamental response is observed in the power spectrum (see Figure. 30a). This corresponding portion of the signals represented in Figure. 30, is classified as region A.

In contrast, the A_{pk-pk} values of the backscattered signals at high pressure varied with time, which is characterized with three regions as B, C and D. We matched these characteristic regions with the single PVA-MB radial oscillation (see Figure. 30).

In region B, the A_{pk-pk} voltage gradually increases with consecutive high-energy bursts and reaches a maximum. In region C, the A_{pk-pk} voltage decreases exponentially due to gas escape from the MB, as seen in the optical images. During this process, the PVA-MBs exhibit violent oscillations, so sub- or ultra-harmonic frequency responses appear in the acoustic emission (see Figure. 31). Finally, the A_{pk-pk} voltage reaches a plateau in region D, which represents the backscattered signals from the gasless PVA shells. The optical experiments confirm this finding with the absence of radial oscillations in the broken PVA-MBs (see Figure. 30). The corresponding power spectrum has integer multiples of the harmonic frequencies, similar to the case of linear scatters subjected to shock waves (see Figure. 3d).
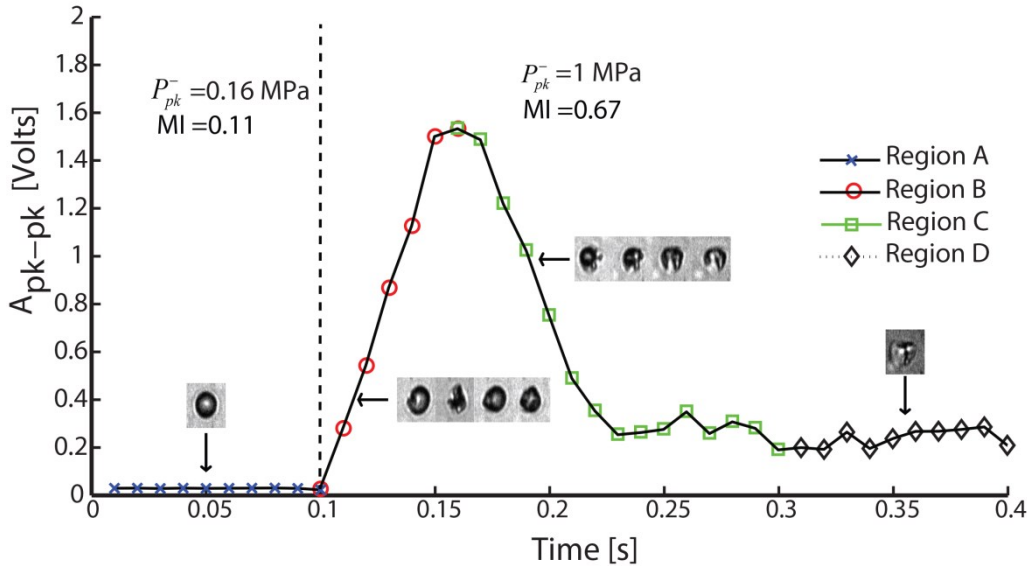
Figure 30. Average peak-to-peak amplitude of the scattered signal upon insonation by an incident pulse with a pressure of about 1 MPa at PRF equal to 100 Hz. Four characteristic regions A, B, C, and D are highlighted.
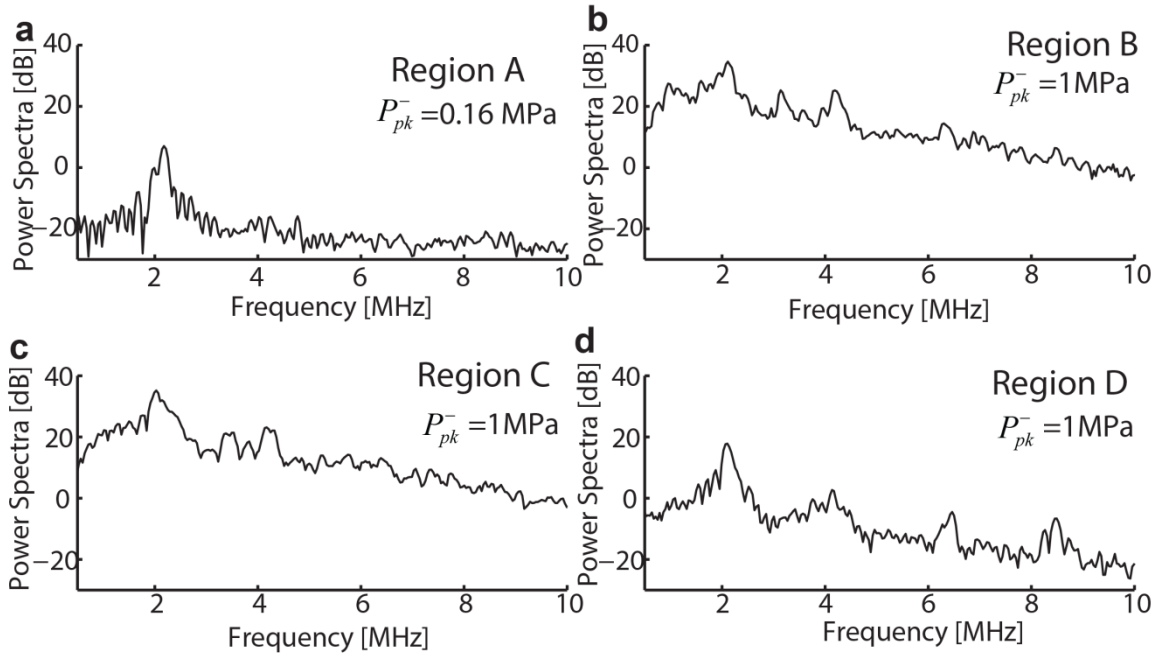
Figure 31. Average power spectra of the backscattered signals at corresponding regions (A, B, C, and D) illustrated in Figure. 30.

5.4 Acoustophoresis

In this section, we present the results of the translatory motion of PVA-MBs in an acoustic standing-wave field at different voltages across the PZT. These results are adopted from Paper 6 and relate to object 4. The primary radiation force drags the solid polymer beads to pressure node planes ($w/4$ and $3w/4$) (see Figure. 32a), whereas the PVA-MBs are driven towards the pressure antinode planes at the center and walls ($w/2$, 0, w) (see Figure. 32b). Once the PVA-MBs are driven to the pressure antinode planes, they group together and aggregate at different locations transverse to the direction of the radiation force. In contrast to PVA-MBs, the solid polymer beads bind to each other and remain as almost a straight pattern along the channel at the pressure nodes.

Both particles (solid polymer beads and PVA-MBs) inside the microchip appear to be black dots against the bright background. Based on the black dot particles, we tracked the intensity profiles at different time intervals (see Figure. 33). Note that the intensity profiles at the edges of the chamber are not included because the differences in intensity between the particles and wall are not distinguishable. As time progressed, the intensity value of polymer microbeads at the pressure node (see Figure. 33a) and the intensity value of the PVA-MBs at the pressure antinode (see Figure. 33c) increased.
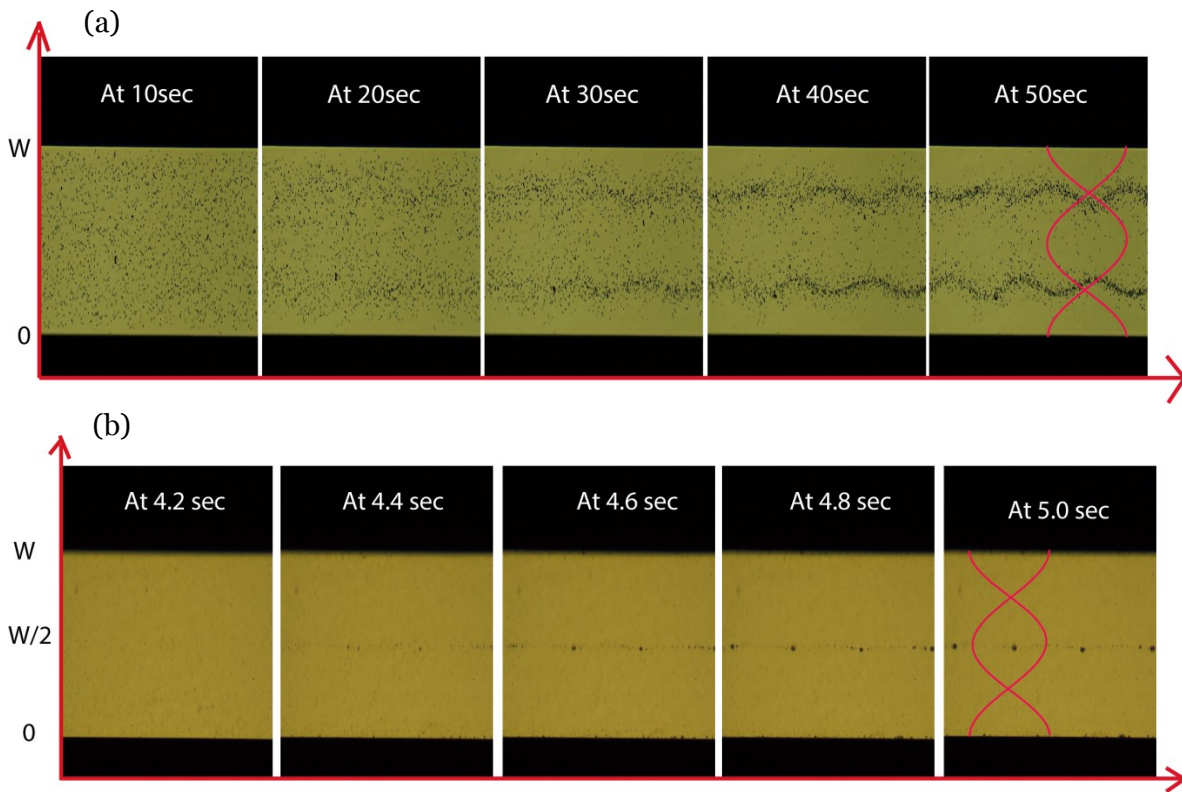
Figure 32. Microscopic images focused on the long rectangular chamber channel (a) 5 μm blood phantoms (represented by black dots) positioned at w/4, 3w/4 and (b) PVA-MBs positioned at the pressure antinode planes (0, w/2, w). Here the electrical potential across the PZT was equal 10 volts.

Table 5. Data of accumulation time of microbeads at pressure node and microbubbles at pressure anti-nodal plane with respect to the driving voltage across the PZT.

Electrical potential [V]	Polymer microbeads accumulation time at pressure node [s]	PVA-MBs accumulation time at pressure antinode [s]
1	-	37
2	-	10
3	188	4.7
4	105	2.1
5	74	1.6
6	54	1.4
7	47	1.0
8	31	0.7
9	30	0.6
10	26	0.5

The accumulation time of these particles are traced by selecting the region of interest (ROI) at the pressure node (see Figure. 33b) and at the pressure antinode (Figure. 33d). The

intensity of both types of particles increases with the activation of the PZT and reaches a maximum. Later, the intensity curve becomes saturated at the maximum intensity value. The time difference between the PZT activation and the maximum intensity value is identified as the "accumulation time". As mentioned above, we calculated the accumulation time of both the solid polymer beads and PVA-MBs at different electrical potentials across the PZT (see Table 5). It is evident that the accumulation time decreases as the electrical potential across the PZT increases. There is no primary radiation effect on the microbeads when the voltage across the PZT is less than 3 volts. At 10 volts, the PVA-MBs are driven to the pressure antinode planes within half a second, whereas the microbeads take approximately 26 sec.
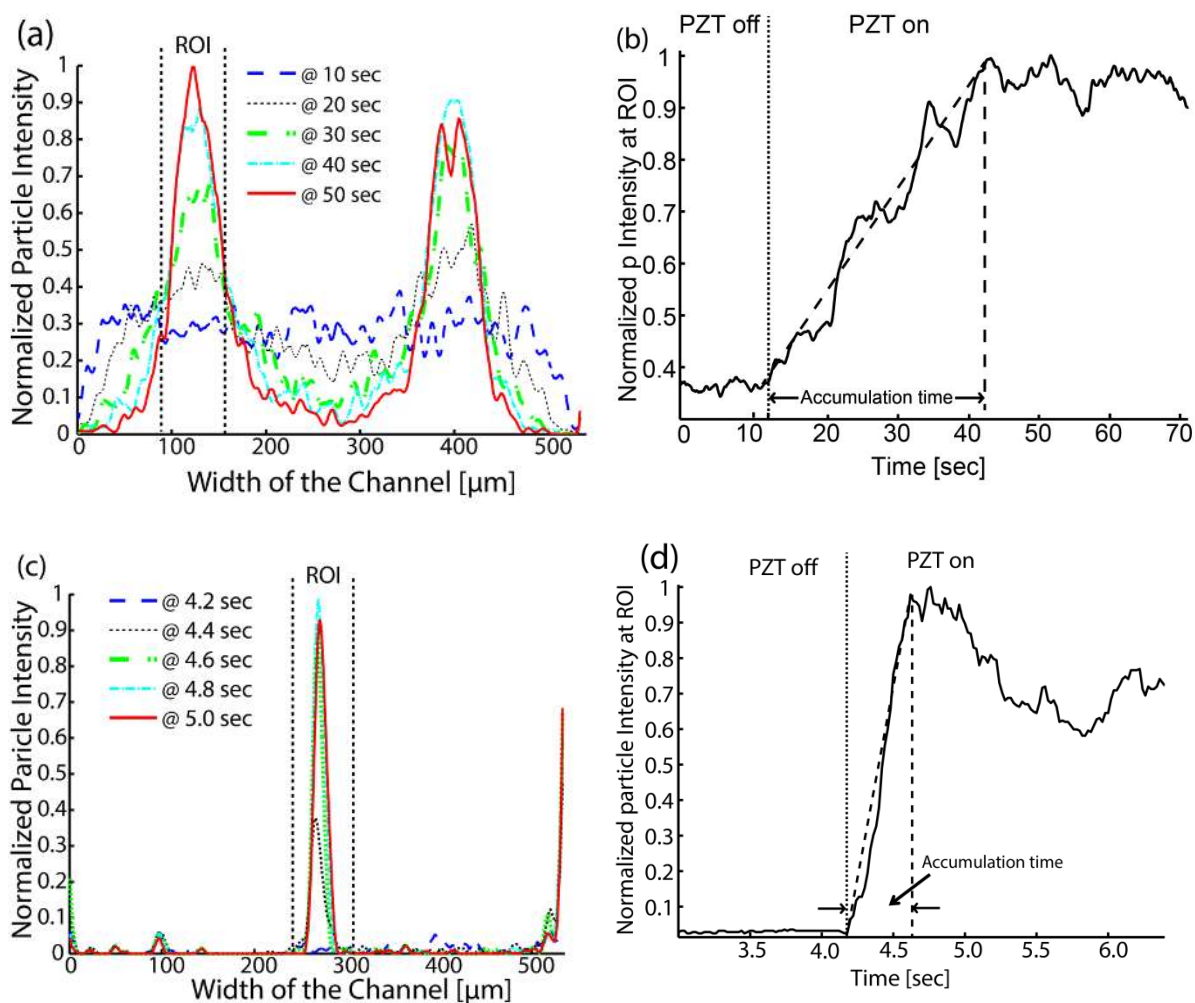
Figure 33. Distributions of (a) solid polymer microbeads and (c) PVA-MBs across the rectangular chamber at different time intervals (before and after the PZT activation). Tracing the maximum intensity values (b) at the pressure node, i.e., at 133±40 μm, and (d) at the pressure antinode, i.e., at 268±40 μm, to calculate the accumulation time of the particles.

6. DISCUSSION

In this chapter, the results presented in this thesis and the relevant clinical applications are discussed.

6.1 Acoustic characterization

In this section, the results of the acoustic characterization of the modified PVA-MBs with respect to the unmodified PVA-MBs are discussed. These discussions cover object 1.

6.1.1 Backscattering power

The commercial UCAs in the blood pool generate a BSP of >20 dB above the noise floor, which provides an opportunity to detect the echo signals from the blood and differentiate from the surrounding tissue [66, 67]. We observed 20 dB BSP enhancements when the number of MBs-chem at the investigated volume is approximately 4.4×10^5 MBs/ml and the number of MBs-phys is approximately 2.0×10^6 MBs/ml (see Figure. 21). The plain PVA-MBs showed an approximately 20 dB BSP enhancement when the number of PVA-MBs is approximately 3.7×10^5 MBs/ml [9]. Thus, it can be concluded that for fixed concentrations, MBs-phys provided less BSP enhancement than either MBs-chem and plain PVA-MBs. According to the Rayleigh scattering mentioned in Eq. 1, the BSP should increase with the number particles in the measured volume, N. However, the BSP of MBs-chem decreases when the concentration is above 8.8×10^5 MBs/ml due to the multiple reflection effect. Similar findings were reported [68] in the case of Albunex® (protein-shelled MBs) particles when the concentration is more than 10^6 MBs/ml. On the other hand, MBs-phys follows the Rayleigh scattering, and the BSP increases as the number of MBs-phys in the insonified volume increases. Thus, MBs-phys behave like rigid particles with a density substantially different from that of the surrounding media. Hence, the MBs-chem is acoustically more active than MBs-phys. The BSP enhancement of MBs-chem is always 4-6 dB higher than MBs-phys below a concentration of 10^6 MB/ml. Similar findings were reported by an imaging group (EsaoteSPA, Italy), where the CTR of MBs-chem is 6 dB above the CTR of

MBs-phys at a concentration of 5×10^5 MBs/ml and a pressure of 450 kPa (see Figure 8 in the appended Paper 2).

The MRI study on MBs-chem and MBs-phys confirmed that both MBs-chem and MBs-phys can be traced in MR imaging as negative contrast media. MBs-phys have an approximately 43% higher net magnetization than MBs-chem, but the number of SPION nanoparticles in the MBs-phys (15 %) is approximately two-fold lower than in MBs-chem (29 %) (see Paper 1). Thus, MBs-phys is a better MR contrast agent than MBs-chem.

6.1.2 Attenuation coefficient and phase velocity

The results of the attenuation coefficient and phase velocity at different dilutions (see Figures. 22a and 22b) show in both MBs that the attenuation coefficient increases and the phase velocity decreases linearly with respect to concentration. At a high concentration of 1.75×10^6 MB/ml, a 20 dB/cm attenuation coefficient and a large dispersion in the phase velocity were found in MBs-chem. On the other hand, the acoustic wave passes through the MBs-phys with lower attenuation and distortion, even at 4.0×10^6 MB/ml (see Figure. 22b). The contrast-enhanced ultrasound is combined with the power Doppler technique to identify the Doppler shift in the estimation of the myocardium velocity [69]. The distortions in the wave propagation through the MB suspensions cause overestimation of the myocardium velocity. This drawback could be overcome using MBs-phys because they contribute fewer artifacts to the incidental wave, even at high concentrations.

Note that in the ideal condition, both the attenuation coefficient and phase velocity values of the MBs should be as close possible to values of soft tissue, which are between 0.3-1.0 dB/(cm×MHz) [70] and 1494 m/s at 24ºC respectively, to avoid shadowing artefacts during the visualization of the distal parts of organs (a more elaborate discussion is provided in Paper 2). As the concentration of MBs in the region of the investigated volume increases, the BSP enhancement increases (positive effect) and attenuation and distortion obstruct the visualization of the bottom plane of the organ (adverse effect). In addition, there is also a clinically recommended upper threshold of MBs inside the body, which should be below 2×10^6 MBs/ml. By considering the above limitations and recommendations, we have chosen concentrations of 8.8×10^5 MBs/ml and 2×10^6 MBs/ml for MBs-chem and MBs-phys respectively, as an optimal concentration to consider for contrast-enhanced Doppler ultrasound investigations.

6.1.3 Fracture pressure threshold

The ultrasound-induced fracture threshold of MBs-chem decreases as the number of cyclic loading increases (see Figure. 24). The accumulation of damage within the shell might be the reason for the facilitation of the fracture progression with cyclic loading. Similar trends were previously identified in unmodified PVA-MBs [71] and also in polymeric BiSpheres-0.7 MBs [72]. These results are also in good agreement with the results of ultrasound imaging (see Figure 7 in appended Paper 2). At a pressure of approximately 450 kPa, the MBs-chem are significantly fractured when they are excited with chirp CPS3 pulses rather than chirp excitations alone. Chirp CPS3 consists of three pulses, and each pulse consists of 45 cycles. The P_{thr} value of MBs-phys does not change at N= 8, 10 and 12 cycles. This behavior portrays the MBs-phys as a rigid particle compared with MBs-chem, and its fracturing is dependent on only pressure (see Paper 2 for a detailed description).

6.2 Modeling

To understand the difference in the acoustical responses of MBs-chem and MBs-phys, we further investigated the mechanical properties through the modeling of the acoustic attenuation coefficient and phase velocity spectra within the frequency range of 3-12 MHz. Indeed, the shell mechanical properties are vital in performing ultrasound contrast imaging [15]. Mechanical parameters, i.e., storage modulus, G', and loss modulus, G'', were obtained by calculating the (1) extinction cross-section, σ_e (used in Paper 3) and (2) the equation of the speed of sound in a bubbly liquid (used in Paper 4). In both studies, relatively lower G' and G'' values are obtained for MBs-chem than for MBs-phys or PVA-MBs. Thus, the stiffness of the MBs are in the order of MBs-chem < plain MBs < MBs-phys (see Table 3). These results are in good agreement with quasi-static force measurements, in which the elastic modulus of MBs-chem (0.23 MPa) was found to be well below the elastic modulus of both the plain PVA-MBs (1.3 MPa) and MBs-phys (3.2 MPa) (see Paper 3 for a more detailed description).

As mentioned in Eq. 19 and 20, the storage modulus, G', and the loss modulus, G'', are directly proportional to the R_{02}, and the ρ_s, and inversely proportional to the shell thickness. In addition, G', is proportional to the square of the ω_0 and G'' is proportional to the δ_s.

$$G' = \frac{R_{02}^3}{4V_S}\left[\alpha\rho_S R_{01}^2 \omega_0^2 - 3\kappa R_{02}^3 P_{G,eq}\right] \quad (19) \qquad G'' = \frac{R_{02}^3}{4V_S}R_{01}^2\alpha\rho_S\delta_S \quad (20)$$

From the atomic force microscope (AFM) measurements, the average radius (1.8±0.8 μm) and average shell thickness (215±133 nm) are equal for all MBs. Thus, the radius and shell thickness values are constant for all MBs. The shell density, ρ_s, varies between MBs in the order of MBs-chem (1774 kg/m³) < MBs-phys (1393 kg/m³) < plain MBs (1054 kg/m³). Note that the density of the shell was calculated based on the percentage of PVA molecules and the water molecules and the number of SPIONs within the shell. Undoubtedly, the density of the shell plays a role in the acoustical properties of MBs, but in this case, both the mechanical and acoustical properties confirm that the softer shell of MBs-chem than that of MBs-phys is primarily due to the SPION conjugation strategy.

It can be observed that the estimated viscoelastic parameter values differed from Paper 3 to Paper 4, even though we used the same measurement data for modeling. The ambiguity in the estimation of the viscoelastic parameters is because different shell thickness and diameter values were used in Papers 3 and 4, as mentioned in Table 2. Moreover, in Paper 2, only the attenuation profile data set was used to predict the four unknown variables (G_{eq}, G_1, μ_{eq}, and μ_1), whereas in Paper 3, the phase velocity data set was included along with the attenuation coefficients to predict the four unknown variables. For this reason, we obtained different viscoelastic parameters (see Tables 3 and 4).

The resonance frequency and damping ratio parameters hold the key for performing the ultrasound contrast-enhanced imaging at different frequencies and also to determine the radial oscillations of MBs at different frequencies. In previous studies, the resonance frequency can be identified through a visual inspection, in which the damped resonance frequency is evident in the attenuation spectra as a sharp peak [17, 73]. However, in the cases of MBs-chem and MBs-phys, there is no sign of a resonance peak in either the

attenuation coefficient or phase velocity spectra. The attenuation coefficient and phase velocity spectra (see Figure 4 in Paper 4) are flat and dampen the resonance frequency peak, as in plain PVA-MBs [9]. Grishenkov et al. identified the radial resonance frequency, ω_0, of plain PVA-MBs (approximately 100 MHz) by fitting the measured attenuation coefficient spectra with the theoretical modeling [9]. The estimated resonance frequency of MBs-chem was approximately 11 MHz, which is below the limit of the diagnostic ultrasound frequency range, i.e., 1-15 MHz. Thus, the MBs-chem can be potentially exploited as a conventional ultrasound contrast agent with the additional functionality of MRI detection. In contrast, the resonance frequency of MBs-phys was found to be approximately 28 MHz, which is far above the diagnostic ultrasound frequency limit. Further modification of the clinically available contrast pulse sequences is required to visualize the MBs-phys, as described in Paper 2.

The damping ratio, ζ_{tot}, represents the oscillatory behavior of the MBs post-excitation (i.e., after ultrasound pulse excitation). Depending on the magnitude of ζ_{tot}, the post-oscillations of the system can be classified as one of three types [74]:

(i) underdamped harmonic oscillator for $\zeta_{tot}<1$ (after post-excitation, the MB oscillates radially in a sinusoidal fashion around its equilibrium, with the gradual reduction of amplitude),

(ii) critically damped harmonic oscillator for $\zeta_{tot}=1$ (MB radial oscillation returns quickly to equilibrium without oscillations), and

(iii) overdamped harmonic oscillator for $\zeta_{tot}>1$ (MB radial oscillation returns to equilibrium in an exponential manner).

The ζ_{tot} values of the unmodified PVA-MBs and MBs-phys at 10 MHz (driving frequency) are identified just over unity (see Figure. 27b and c), which are considered to be overdamped harmonic oscillator systems. On the other hand, the ζ_{tot} of MBs-chem is found to be just below 1 (see Figure. 27a), so post-excitation radial oscillations are expected in MBs-chem. Indeed, the magnitude of these post-excitation radial oscillations could be minor compared to that of the phospholipid-shelled MBs due to the high damping. The ζ_{tot} of phospholipid-shelled UCAs is well below 1 (see Figure. 27d), classifying them as underdamped harmonic oscillator. For this reason, phospholipid-shelled MBs are acoustically active, and the post-excitation oscillations were confirmed by Morgan et al., who observed radial oscillations of phospholipid-MBs in streak images even after the removal of the excitation pulse [75].

The above discussions (from Papers 1, 2, 3 and 4) leads to the conclusion that the SPION arrangement in the PVA shell plays a significant role in obtaining optimal good acoustical and magnetic properties. This can be explained by the cross-linking theory, which describes the stiffness of the cross-linked network. The crosslink stiffness is directly proportional to the filament length and the cross-linker concentration [76]. The SPIONs on the PVA surface (in MBs-chem) could act as an additional preload to cross-link the network upon ultrasound exposure. On the other hand, SPION particles inside the PVA shell (in MB-phys) could serve as additional linkers to the cross-linked PVA network, and the resulting shell could act as a composite or bundle cross-linked network. This assumption is in good agreement with the differential scanning calorimetry (DSC)

measurements wherein a loss of the crystalline structure in the cross-link network was observed in MBs-chem (see Figures 4 and 5 in Paper 1) but not in MBs-phys. Thus, MBs-chem's shell behaves as a softer shell and MBs-phys behaves as a hard shell under the ultrasound exposures.

Finally, the above findings reveal that the acoustic properties can be altered by SPIONs attachment, and similar findings were reported by He et al. [77].

6.3 Nonlinear oscillations and ultrasound-induced fracture mechanism

Pecorari et al. [71] used backscattered time domain signals to describe the fracturing mechanism of plain PVA-MBs, which is a more indirect method of understanding fracturing events. Direct visualization gives a complete insight into the fracturing mechanism of MBs, which is essential for high intensity ultrasound contrast-enhanced imaging applications. The real-time images of the radial oscillation of individual PVA-MBs at high power ultrasound bursts are presented in Figures. 28and 29. Approximately at the same pressures, the backscattered time domain signals from the PVA-MB suspension are also complemented by the visualization results. The optical recordings of the PVA-MBs reveal that the air core is extruded through several cracks, although the leaking of gas molecules into the surrounding liquid is not visualized. This fracturing mechanism is different from the previously reported fracturing behavior of MBs [33, 78]. These observations are in good agreement with the acoustic examinations at high power bursts, in which the backscattered peak-to-peak voltages from the population of MBs with respect to insonation pulses gradually increase and reach a maximum before decreasing exponentially. The results of both experimental observations show that the PVA-MBs cannot be disrupted with a single ultrasonic burst of high power (where MI=0.67), but rather require several closely spaced bursts. We presume that the gas is squeezed out through the pores of the complex PVA shell [51] rather than through cracks. The diameter of the MBs reduces with an increased number of insonation pulses, similar to lipid-shedding behavior [44]. We refer to this gas-shedding behavior as "pumping-out" behavior, and it is characterized by the presence of second-, ultra- and sub-harmonics (see Figures. 31c and 31d). The fractured PVA shell remains intact after all of the gas molecules have left the core, which makes it attractive for ultrasound molecular therapeutic purposes.

As shown in Figure. 30, the fracturing events of MBs are classified into four (A, B, C, and D) regions. In the myocardial perfusion study with MBs, "region B" was observed as a step function for both the thin-shelled phospholipid MBs [32] and thick-shelled polymer MBs [79]. To date, region B in the "pumping-out" mechanism has not reported anywhere else. A train of high power ultrasound bursts with a short interval or a nonconventional pulse sequence such as Chirp techniques should be used to study the tissue-perfusion study with PVA-MBs [10]. The "pumping-out" behavior can be used efficiently and selectively deliver therapeutic gases (such as nitric oxide, NO) loaded into PVA-MBs[56]. The imaging of PVA-MBs at fundamental or second harmonic frequencies was not successful, even at high pressures [10]. The PVA-MBs exhibit buckling modes of oscillation at high-pressure amplitude excitations, which generates sub- or ultra-harmonics. Hence, imaging at sub- or ultra- harmonics in PV-MBs would benefit the detection of low concentrations of PVA-MBs (down to a single PVA-MB) in micro-capillaries.

6.4 Acoustophoresis

In this work, we investigated the translatory motion of the PVA-MBs and solid polymer beads caused by the radiation force in an acoustic standing-wave field. The following discussions are part of study objective 4.

The acoustic contrast factor, Φ, of the PVA-MBs was calculated to be approximately -60.7. Thus, according to theory, the PVA-MBs are supposed to migrate towards the pressure antinode. The experimental results confirm the theoretical predictions that the PVA-MBs are translated and accumulated at the pressure antinode planes. The PVA-MBs' motion in acoustic standing-wave fields is similar to that of negative acoustic contrast particles such as lipid (fat) particles [80], oil droplets [81], elastomeric particles [82] and hollow particles [83]. The Φ of blood cells, microbeads, lipid particles, oil droplets and elastomeric particle is less than unity, because their density and compressibility difference from the surrounding fluid media are not significant. However, in the PVA-MBs, the compressibility difference of the gas core is several orders higher than that of the surrounding fluid media. As a result, we observed a higher Φ value. The radiation force, F_{rad}^{y}, is directly proportional to the volume of the particle, V, the square of the pressure amplitude, p^2, the frequency, f, and the acoustic contrast factor, Φ. However, the volume of the microbeads (5.23×10^{-16}) is 2.2 times higher than volume of the PVA-MBs (2.29×10^{-16}) [84], but the large Φ causes the PVA-MBs to be relocated much faster than the microbeads (given in Table 5). The resonance effect significantly changes the motion of the gas bubbles [85]. In this study, the driving frequency (2.8 MHz) is well below the resonance frequency (12 MHz) of the PVA-MBs [9], so the pulsations of the MBs are in-phase with the incidental wave.

As shown in Figure. 33, it is possible that PVA-MBs (negative acoustic contrast particles) can be separated from erythrocytes, leukocytes or tissue cells (positive acoustic contrast particles). In addition, the PVA-MBs require much lower power to manipulate than plain polymer beads or cells. Thus, at low acoustic pressures, the targeted PVA-MBs binding with cells can be trapped at the pressure antinode planes where the free cells cannot be affected. Moreover, the acoustophoresis method requires only little samples, which is an added advantage. Thus, the investigation of the bioclearance or bioassay studies of PVA-MBs *in vitro* using acoustophoresis would be feasible and economical.

7. CONCLUSIONS

The objectives given in the Chapter 2 have been successfully addressed. This work contributes significant feedback to chemist group (to optimize nanoparticle inclusion) and imaging groups (to develop new imaging sequences), and the positive findings pave new paths and suggested triggers for further research. The specific conclusions based on the key findings of this thesis are summarized below:

– The modified magnetic MBs possess a similar acoustical response to unmodified PVA-MBs, but they mainly rely on an inclusion strategy. If the SPIONs are included on the surface of the PVA shell, then the modified MBs become softer and exhibit a better acoustical response, whereas if the SPIONs are included inside the PVA shell, then they behave as hard-shelled MBs.

– The overall acoustical, mechanical, physical, magnetic, and ultrasound imaging performance of modified and unmodified PVA-MBs are interpreted as: (1) BSP (MBs-chem≈PVA-MBs>MBs-phys); (2) Absorption (MBs-chem≈PVA-MBs>MBs-phys); (3) shell mechanical properties (MBs-chem<PVA-MBs<MBs-phys); (4) oscillatory properties (MBs-chem<PVA-MBs<MBs-phys); (5) resonance frequency (MBs-chem<PVA-MBs<MBs-phys); (6) ultrasound imaging (MBs-chem<MBs-phys) (6) number of SPIONs (MBs-chem>MBs-phys); (7) magnetization (MBs-chem <MBs-phys).

– For Doppler ultrasound imaging applications, the concentration of the administration solution should contain 8.0×10^5 MBs/ml for MBs-chem and 2.0×10^6 MBs/ml for MBs-phys to obtain the optimal SNR with minimal artefacts. Both MBs-chem and MBs-phys can be visualized with ultrasound and MRI probes with the help of special pulse excitation techniques combined with signal processing methods.

– Thus, dual modality contrast agents MBs-chem and MBs-phys are useful as a single contrast injection for simultaneous US and MR contrast-enhanced imaging to acquire anatomical and structural information (objectives 1 and 2 are concluded).

– The fracturing mechanism of PVA-MBs (where the gas was slowly extruded through several pores in the PVA shell like the crenation in cells following several high power bursts) is identified to be unique and not observed in other types of MBs. The fracturing mechanism of the PVA-MBs is referred to "pumping-out behavior", and it can be used in site-specific therapeutic gas delivery. Moreover, during the process of gas extrusion, the PVA-MBs exhibit other modes (produces sub- and ultra- harmonics) of oscillation upon a high power burst. The isolation of buckling mode oscillations might provide an opportunity to obtain single PVA-MB imaging (objective 3 is concluded).

– The PVA-MBs can be actuated at a very low acoustic pressure at which solid polymer beads do not respond. The PVA-MBs can also be distinguishable from similarly sized solid particles. This study indicates that the PVA-MBs can even be separated from blood cells (objective 4 is concluded).

8. FUTURE WORK

In this section, new ideas and future research questions based on the findings of this work are suggested:

– The stiffness and load-bearing capacities of magnetostrictive gels varies in the presence of a magnetic field. The stiffness parameters increase with the magnetic flux [86]. In this thesis, the viscoelastic properties of modified PVA-MBs were estimated without the presence of an external magnetic field, and it was found the acoustical properties of MBs change with the stiffness. If the modified PVA-MBs vary their stiffness under the presence of an external magnetic field, then contrast-enhanced US imaging should be the first choice over MRI. Hence, it would be interesting to assess the acoustical properties of modified PVA-MBs under the presence of external magnetic fields with varying magnetic flux.

– As was mentioned in the Discussion chapter section 6.3, the buckling modes of oscillation (which produce the sub- and ultra-harmonics) of PVA-MBs at high pressures is another great finding of this thesis. Imaging at the sub- or ultra- harmonic frequencies not only exhibits an improved CTR ratio, but is also crucial for molecular imaging when the single MB detection is necessary. Thus, it is of great interest for further studies.

– Recently, our group has shown that the therapeutic gasses, such as nitric oxide (NO), can be replaced with air core in the PVA-MBs [56]. Thus, the potential therapeutic gas delivery capabilities should be tested with the "pumping-out" fracturing mechanism.

– The results of this preliminary study on the motion of PVA-MBs in a standing wave acoustic field should be extended to study the precise manipulation at different frequencies and different pressures. Moreover, cell behaviors in the presence of MBs should also be studied.

REFERENCES

[1]   R. Gramiak and P. M. Shah, "Echocardiography of the aortic root," *Investigative radiology,* vol. 3, pp. 356-366, 1968.

[2]   B. B. Goldberg, J.-B. Liu, and F. Forsberg, "Ultrasound contrast agents: a review," *Ultrasound in medicine & biology,* vol. 20, pp. 319-333, 1994.

[3]   N. De Jong, F. Ten Cate, C. Lancee, J. Roelandt, and N. Bom, "Principles and recent developments in ultrasound contrast agents," *Ultrasonics,* vol. 29, pp. 324-330, 1991.

[4]   S. B. Feinstein, P. M. Shah, R. J. Bing, S. Meerbaum, E. Corday, B.-L. Chang, *et al.*, "Microbubble dynamics visualized in the intact capillary circulation," *Journal of the American College of Cardiology,* vol. 4, pp. 595-600, 1984.

[5]   M. Schneider, "SonoVue, a new ultrasound contrast agent," *European radiology,* vol. 9, p. S347, 1999.

[6]   M. A. Wheatley, B. Schrope, and P. Shen, "Contrast agents for diagnostic ultrasound: development and evaluation of polymer-coated microbubbles," *Biomaterials,* vol. 11, pp. 713-717, 1990.

[7]   A. Martegani19, S. Meairs20, C. Nolsøe21, F. Piscaglia22, P. Ricci23, G. Seidel24, *et al.*, "Guidelines and Good Clinical Practice Recommenda-tions for Contrast Enhanced Ultrasound (CEUS)–Update 2008," 2008.

[8]   X. Cai, F. Yang, and N. Gu, "Applications of magnetic microbubbles for theranostics," *Theranostics,* vol. 2, p. 103, 2012.

[9]   D. Grishenkov, C. Pecorari, T. B. Brismar, and G. Paradossi, "Characterization of acoustic properties of PVA-shelled ultrasound contrast agents: linear properties (part I)," *Ultrasound in medicine & biology,* vol. 35, pp. 1127-1138, 2009.

[10]   C. Sciallero, G. Paradossi, and A. Trucco, "A preliminary in vitro assessment of polymer-shelled microbubbles in contrast-enhanced ultrasound imaging," *Ultrasonics,* vol. 52, pp. 456-464, 2012.

[11]   M. Tortora, L. Oddo, S. Margheritelli, and G. Paradossi, "Design of Novel Polymer Shelled Ultrasound Contrast Agents: Towards an Ultrasound Triggered Drug Delivery," in *Ultrasound Contrast Agents*, ed: Springer, 2010, pp. 25-39.

[12]   C. T. Chin, C. Lancée, J. Borsboom, F. Mastik, M. E. Frijlink, N. de Jong, *et al.*, "Brandaris 128: A digital 25 million frames per second camera with 128 highly sensitive frames," *Review of scientific instruments,* vol. 74, pp. 5026-5034, 2003.

[13]   P. R. Hoskins, K. Martin, and A. Thrush, *Diagnostic ultrasound: physics and equipment*: Cambridge University Press, 2010.

[14]   T. Neuman, D. Hall, and P. Linaweaver Jr, "Gas phase separation during decompression in man: ultrasound monitoring," *Undersea biomedical research,* vol. 3, p. 121, 1976.

[15] L. Hoff, *Acoustic characterization of contrast agents for medical ultrasound imaging*: Springer, 2001.

[16] O. I. Soliman, M. L. Geleijnse, F. J. Meijboom, A. Nemes, O. Kamp, P. Nihoyannopoulos*, et al.*, "The use of contrast echocardiography for the detection of cardiac shunts," *European Journal of Echocardiography,* vol. 8, pp. s2-s12, 2007.

[17] N. De Jong, M. Emmer, A. Van Wamel, and M. Versluis, "Ultrasonic characterization of ultrasound contrast agents," *Medical & biological engineering & computing,* vol. 47, pp. 861-873, 2009.

[18] H. Becher and P. N. Burns, *Handbook of contrast echocardiography: Left ventricular function and myocardial perfusion*: Springer Verlag, 2000.

[19] P. N. Burns and H. Becher, "Handbook of contrast echocardiography," ed: Frankfurt: Springer Verlag, 2000.

[20] G. Tortora and S. Grabowski, "Introduction of the Human Body, The Essentials of Anatomy and Physiology, Japanese translation by Maruzen Co," ed: Ltd, 2004.

[21] S. T. Reddy, A. J. van der Vlies, E. Simeoni, V. Angeli, G. J. Randolph, C. P. O'Neil*, et al.*, "Exploiting lymphatic transport and complement activation in nanoparticle vaccines," *Nature biotechnology,* vol. 25, pp. 1159-1164, 2007.

[22] G. Ter Haar, "Safety and bio-effects of ultrasound contrast agents," *Medical & biological engineering & computing,* vol. 47, pp. 893-900, 2009.

[23] S. Sirsi and M. Borden, "Microbubble compositions, properties and biomedical applications," *Bubble Science, Engineering & Technology,* vol. 1, pp. 3-17, 2009.

[24] T. Faez, M. Emmer, K. Kooiman, M. Versluis, A. F. van der Steen, and N. de Jong, "20 years of ultrasound contrast agent modeling," *Ultrasonics, Ferroelectrics and Frequency Control, IEEE Transactions on,* vol. 60, 2013.

[25] D. H. Simpson, C. T. Chin, and P. N. Burns, "Pulse inversion Doppler: a new method for detecting nonlinear echoes from microbubble contrast agents," *Ultrasonics, Ferroelectrics, and Frequency Control, IEEE Transactions on,* vol. 46, pp. 372-382, 1999.

[26] R. J. Eckersley, C. T. Chin, and P. N. Burns, "Optimising phase and amplitude modulation schemes for imaging microbubble contrast agents at low acoustic power," *Ultrasound in medicine & biology,* vol. 31, pp. 213-219, 2005.

[27] P. Phillips, "Contrast pulse sequences (CPS): imaging nonlinear microbubbles," in *Ultrasonics Symposium, 2001 IEEE*, 2001, pp. 1739-1745.

[28] K. Tiemann, C. Veltmann, A. Ghanem, S. Lohmaier, M. Bruce, S. Kuntz-Hehner*, et al.*, "The impact of emission power on the destruction of echo contrast agents and on the origin of tissue harmonic signals using power pulse-inversion imaging," *Ultrasound in medicine & biology,* vol. 27, pp. 1525-1533, 2001.

[29] H. Shekhar and M. M. Doyley, "Improving the sensitivity of high-frequency subharmonic imaging with coded excitation: A feasibility study," *Medical physics,* vol. 39, pp. 2049-2060, 2012.

[30] T. Faez, M. Emmer, M. Docter, J. Sijl, M. Versluis, and N. de Jong, "Characterizing the subharmonic response of phospholipid-coated microbubbles for carotid imaging," *Ultrasound in medicine & biology,* vol. 37, pp. 958-970, 2011.

[31] R. Senior, S. Kaul, P. Soman, and A. Lahiri, "Power Doppler harmonic imaging: a feasibility study of a new technique for the assessment of myocardial perfusion," *American heart journal,* vol. 139, pp. 245-251, 2000.

[32] K. Wei, A. R. Jayaweera, S. Firoozan, A. Linka, D. M. Skyba, and S. Kaul, "Quantification of myocardial blood flow with ultrasound-induced destruction of microbubbles administered as a constant venous infusion," *Circulation,* vol. 97, pp. 473-483, 1998.

[33] S. H. Bloch, M. Wan, P. A. Dayton, and K. W. Ferrara, "Optical observation of lipid-and polymer-shelled ultrasound microbubble contrast agents," *Applied Physics Letters,* vol. 84, pp. 631-633, 2004.

[34] K. Kooiman, M. R. Böhmer, M. Emmer, H. J. Vos, C. Chlon, W. T. Shi*, et al.*, "Oil-filled polymer microcapsules for ultrasound-mediated delivery of lipophilic drugs," *Journal of Controlled Release,* vol. 133, pp. 109-118, 2009.

[35] D. L. Miller, M. A. Averkiou, A. A. Brayman, E. C. Everbach, C. K. Holland, J. H. Wible, *et al.*, "Bioeffects considerations for diagnostic ultrasound contrast agents," *Journal of Ultrasound in Medicine,* vol. 27, pp. 611-632, 2008.

[36] K. Kooiman, M. Foppen-Harteveld, A. F. van der Steen, and N. de Jong, "Sonoporation of endothelial cells by vibrating targeted microbubbles," *Journal of Controlled Release,* vol. 154, pp. 35-41, 2011.

[37] N. Sheikov, N. McDannold, N. Vykhodtseva, F. Jolesz, and K. Hynynen, "Cellular mechanisms of the blood-brain barrier opening induced by ultrasound in presence of microbubbles," *Ultrasound in medicine & biology,* vol. 30, pp. 979-989, 2004.

[38] C. A. Grant, J. E. McKendry, and S. D. Evans, "Temperature dependent stiffness and visco-elastic behaviour of lipid coated microbubbles using atomic force microscopy," *Soft Matter,* vol. 8, pp. 1321-1326, 2012.

[39] A. A. Doinikov and A. Bouakaz, "Review of shell models for contrast agent microbubbles," *Ultrasonics, Ferroelectrics, and Frequency Control, IEEE Transactions on,* vol. 58, pp. 981-993, 2011.

[40] M. Postema, A. Bouakaz, M. Versluis, and N. de Jong, "Ultrasound-induced gas release from contrast agent microbubbles," *Ultrasonics, Ferroelectrics and Frequency Control, IEEE Transactions on,* vol. 52, pp. 1035-1041, 2005.

[41] D. Lensen, E. C. Gelderblom, D. M. Vriezema, P. Marmottant, N. Verdonschot, M. Versluis, *et al.*, "Biodegradable polymeric microcapsules for selective ultrasound-triggered drug release," *Soft Matter,* vol. 7, pp. 5417-5422, 2011.

[42] P. A. Dayton, K. Morgan, A. Klibanov, G. Brandenburger, and K. Ferrara, "Optical and acoustical observations of the effects of ultrasound on contrast agents," *Ultrasonics, Ferroelectrics and Frequency Control, IEEE Transactions on,* vol. 46, pp. 220-232, 1999.

[43] A. Bouakaz, M. Versluis, and N. de Jong, "High-speed optical observations of contrast agent destruction," *Ultrasound in medicine & biology,* vol. 31, pp. 391-399, 2005.

[44] M. A. Borden, D. E. Kruse, C. F. Caskey, S. Zhao, P. A. Dayton, and K. W. Ferrara, "Influence of lipid shell physicochemical properties on ultrasound-induced microbubble destruction," *Ultrasonics, Ferroelectrics and Frequency Control, IEEE Transactions on,* vol. 52, pp. 1992-2002, 2005.

[45] D. Thomas, M. Butler, T. Anderson, M. Emmer, H. Vos, M. Borden, *et al.*, "The "quasi-stable" lipid shelled microbubble in response to consecutive ultrasound pulses," *Applied Physics Letters,* vol. 101, p. 071601, 2012.

[46] V. S. Kothapalli, "Ultrasound Contrast Agents Loaded with Magnetic Nanoparticles: Acoustic and Mechanical Characterization," 2013.

[47] N. de Jong, L. Hoff, T. Skotland, and N. Bom, "Absorption and scatter of encapsulated gas filled microspheres: theoretical considerations and some measurements," *Ultrasonics,* vol. 30, pp. 95-103, 1992.

[48] C. C. Church, "The effects of an elastic solid surface layer on the radial pulsations of gas bubbles," *The Journal of the Acoustical Society of America,* vol. 97, pp. 1510-1521, 1995.

[49] G. Paradossi, F. Cavalieri, E. Chiessi, C. Spagnoli, and M. K. Cowman, "Poly (vinyl alcohol) as versatile biomaterial for potential biomedical applications," *Journal of Materials Science: Materials in Medicine,* vol. 14, pp. 687-691, 2003.

[50] F. Cavalieri, A. El Hamassi, E. Chiessi, and G. Paradossi, "Stable polymeric microballoons as multifunctional device for biomedical uses: synthesis and characterization," *Langmuir,* vol. 21, pp. 8758-8764, 2005.

[51] G. Tzvetkov, B. Graf, P. Fernandes, A. Fery, F. Cavalieri, G. Paradossi, *et al.*, "In situ characterization of gas-filled microballoons using soft X-ray microspectroscopy," *Soft Matter,* vol. 4, pp. 510-514, 2008.

[52] R. Villa, B. Cerroni, L. Viganò, S. Margheritelli, G. Abolafio, L. Oddo, *et al.*, "Targeted doxorubicin delivery by chitosan-galactosylated modified polymer microbubbles to hepatocarcinoma cells," *Colloids and Surfaces B: Biointerfaces,* vol. 110, pp. 434-442, 2013.

[53] D. Grishenkov, C. Pecorari, T. B. Brismar, and G. Paradossi, "Characterization of acoustic properties of PVA-shelled ultrasound contrast agents: ultrasound-induced fracture (part II)," *Ultrasound in medicine & biology,* vol. 35, pp. 1139-1147, 2009.

[54]   B. Cerroni, E. Chiessi, S. Margheritelli, L. Oddo, and G. Paradossi, "Polymer shelled microparticles for a targeted doxorubicin delivery in cancer therapy," *Biomacromolecules,* vol. 12, pp. 593-601, 2011.

[55]   F. Cavalieri, I. Finelli, M. Tortora, P. Mozetic, E. Chiessi, F. Polizio, *et al.*, "Polymer microbubbles as diagnostic and therapeutic gas delivery device," *Chemistry of Materials,* vol. 20, pp. 3254-3258, 2008.

[56]   D. Grishenkov, G. Adrian, E. Weitzberg, J. Lundberg, J. Harmark, B. Cerroni, *et al.*, "Ultrasound contrast agent loaded with nitric oxide as a theranostic microdevice: Theranostic contrast agent loaded with nitric oxide," *Drug Design, Development and Therapy,* 2014.

[57]   A. P. Sarvazyan, O. V. Rudenko, and W. L. Nyborg, "Biomedical applications of radiation force of ultrasound: historical roots and physical basis," *Ultrasound in medicine & biology,* vol. 36, pp. 1379-1394, 2010.

[58]   L. Rayleigh, "XXXIV. On the pressure of vibrations," *The London, Edinburgh, and Dublin Philosophical Magazine and Journal of Science,* vol. 3, pp. 338-346, 1902.

[59]   J. J. Rychak, A. L. Klibanov, K. F. Ley, and J. A. Hossack, "Enhanced targeting of ultrasound contrast agents using acoustic radiation force," *Ultrasound in medicine & biology,* vol. 33, pp. 1132-1139, 2007.

[60]   A. Lenshof, C. Magnusson, and T. Laurell, "Acoustofluidics 8: Applications of acoustophoresis in continuous flow microsystems," *Lab on a Chip,* vol. 12, pp. 1210-1223, 2012.

[61]   W. Coakley, G. Whitworth, M. Grundy, R. Gould, and R. Allman, "Ultrasonic manipulation of particles and cells. Ultrasonic separation of cells," *Bioseparation,* vol. 4, pp. 73-83, 1994.

[62]   F. Petersson, A. Nilsson, C. Holm, H. Jönsson, and T. Laurell, "Continuous separation of lipid particles from erythrocytes by means of laminar flow and acoustic standing wave forces," *Lab on a Chip,* vol. 5, pp. 20-22, 2005.

[63]   L. Gor'Kov, "On the forces acting on a small particle in an acoustical field in an ideal fluid," in *Soviet Physics Doklady*, 1962, p. 773.

[64]   T. Laurell, F. Petersson, and A. Nilsson, "Chip integrated strategies for acoustic separation and manipulation of cells and particles," *Chemical Society Reviews,* vol. 36, pp. 492-506, 2007.

[65]   T. Huang, J. Burnett, and A. Deczky, "The importance of phase in image processing filters," *Acoustics, Speech and Signal Processing, IEEE Transactions on,* vol. 23, pp. 529-542, 1975.

[66]   J. D. Lathia, L. Leodore, and M. A. Wheatley, "Polymeric contrast agent with targeting potential," *Ultrasonics,* vol. 42, pp. 763-768, 2004.

[67]   S. Lavisse, V. Rouffiac, P. Peronneau, A. Paci, C. Chaix, P. Reb, *et al.*, "Acoustic characterization of a new trisacryl contrast agent. Part I: In vitro study," *Ultrasonics,* vol. 48, pp. 16-25, 2008.

[68]   E. Stride and N. Saffari, "Investigating the significance of multiple scattering in ultrasound contrast agent particle populations," *Ultrasonics, Ferroelectrics, and Frequency Control, IEEE Transactions on,* vol. 52, pp. 2332-2345, 2005.

[69]   M. Ressner, L.-A. Brodin, T. Jansson, L. Hoff, P. Ask, and B. Janerot-Sjoberg, "Effects of ultrasound contrast agents on Doppler tissue velocity estimation," *Journal of the American Society of Echocardiography,* vol. 19, pp. 154-164, 2006.

[70]   P. Wells, "Absorption and dispersion of ultrasound in biological tissue," *Ultrasound in medicine & biology,* vol. 1, pp. 369-376, 1975.

[71]   C. Pecorari and D. Grishenkov, "Characterization of ultrasound-induced fracture of polymer-shelled ultrasonic contrast agents by correlation analysis," *The Journal of the Acoustical Society of America,* vol. 122, pp. 2425-2430, 2007.

[72]   W.-S. Chen, T. J. Matula, A. A. Brayman, and L. A. Crum, "A comparison of the fragmentation thresholds and inertial cavitation doses of different ultrasound contrast agents," *The Journal of the Acoustical Society of America,* vol. 113, pp. 643-651, 2003.

[73]   L. Hoff, P. C. Sontum, and J. M. Hovem, "Oscillations of polymeric microbubbles: Effect of the encapsulating shell," *The Journal of the Acoustical Society of America,* vol. 107, pp. 2272-2280, 2000.

[74]   H. Pain, "Damped Simple Harmonic Motion," *The Physics of Vibrations and Waves, Sixth Edition,* pp. 37-52, 1976.

[75]   K. E. Morgan, J. S. Allen, P. A. Dayton, J. E. Chomas, A. Klibaov, and K. W. Ferrara, "Experimental and theoretical evaluation of microbubble behavior: Effect of transmitted phase and bubble size,"

Ultrasonics, Ferroelectrics, and Frequency Control, IEEE Transactions on, vol. 47, pp. 1494-1509, 2000.

[76] O. Lieleg, M. M. Claessens, and A. R. Bausch, "Structure and dynamics of cross-linked actin networks," *Soft Matter,* vol. 6, pp. 218-225, 2010.

[77] W. He, F. Yang, Y. Wu, S. Wen, P. Chen, Y. Zhang*, et al.*, "Microbubbles with surface coated by superparamagnetic iron oxide nanoparticles," *Materials Letters,* vol. 68, pp. 64-67, 2012.

[78] A. Y. Ammi, R. O. Cleveland, J. Mamou, G. I. Wang, S. L. Bridal, and W. D. O'Brien, "Ultrasonic contrast agent shell rupture detected by inertial cavitation and rebound signals," *Ultrasonics, Ferroelectrics and Frequency Control, IEEE Transactions on,* vol. 53, pp. 126-136, 2006.

[79] P. D. Bevan, R. Karshafian, E. G. Tickner, and P. N. Burns, "Quantitative measurement of ultrasound disruption of polymer-shelled microbubbles," *Ultrasound in medicine & biology,* vol. 33, pp. 1777-1786, 2007.

[80] F. Petersson, A. Nilsson, C. Holm, H. Jönsson, and T. Laurell, "Separation of lipids from blood utilizing ultrasonic standing waves in microfluidic channels," *Analyst,* vol. 129, pp. 938-943, 2004.

[81] H. Wang, Z. Liu, S. Kim, C. Koo, Y. Cho, D.-Y. Jang*, et al.*, "Microfluidic acoustophoretic force based low-concentration oil separation and detection from the environment," *Lab on a Chip,* vol. 14, pp. 947-956, 2014.

[82] C. W. Shields IV, L. M. Johnson, L. Gao, and G. P. López, "Elastomeric Negative Acoustic Contrast Particles for Capture, Acoustophoretic Transport, and Confinement of Cells in Microfluidic Systems," *Langmuir,* vol. 30, pp. 3923-3927, 2014.

[83] I. Leibacher, W. Dietze, P. Hahn, J. Wang, S. Schmitt, and J. Dual, "Acoustophoresis of hollow and core-shell particles in two-dimensional resonance modes," *Microfluidics and Nanofluidics,* vol. 16, pp. 513-524, 2014.

[84] R. Barnkob, P. Augustsson, T. Laurell, and H. Bruus, "Measuring the local pressure amplitude in microchannel acoustophoresis," *Lab on a Chip,* vol. 10, pp. 563-570, 2010.

[85] F. Blake Jr, "Bjerknes forces in stationary sound fields," *The Journal of the Acoustical Society of America,* vol. 21, pp. 551-551, 1949.

[86] M. Farshad and M. Le Roux, "Compression properties of magnetostrictive polymer composite gels," *Polymer testing,* vol. 24, pp. 163-168, 2005.